A Comparison of the Variability and Changes in Global Ocean Heat Content from Multiple Objective Analysis Products During the Argo Period

Xinfeng Liang[1*], Chao Liu[1], Rui M. Ponte[2], Don P. Chambers[3]

1. School of Marine Science and Policy, University of Delaware, Lewes, DE 19958, USA
2. Atmospheric and Environmental Research, Lexington, MA, 02421, USA
3. College of Marine Science, University of South Florida, St Petersburg, FL, 33701, USA

* Corresponding author: Xinfeng Liang (xfliang@udel.edu)

Early Online Release: This preliminary version has been accepted for publication in *Journal of Climate*, may be fully cited, and has been assigned DOI 10.1175/JCLI-D-20-0794.1. The final typeset copyedited article will replace the EOR at the above DOI when it is published.

Abstract

Ocean heat content (OHC) is key to estimating the energy imbalance of the earth system. Over the past two decades, an increasing number of OHC studies were conducted using oceanic objective analysis (OA) products. Here we perform an intercomparison of OHC from eight OA products with a focus on their robust features and significant differences over the Argo period (2005-2019), when the most reliable global scale oceanic measurements are available. For the global ocean, robust warming in the upper 2000 m is confirmed. The 0-300 m layer shows the highest warming rate but is heavily modulated by interannual variability, particularly the El Niño–Southern Oscillation. The 300-700 m and 700-2000 m layers, on the other hand, show unabated warming. Regionally, the Southern Ocean and mid-latitude North Atlantic show a substantial OHC increase, and the subpolar North Atlantic displays an OHC decrease. A few apparent differences in OHC among the examined OA products were identified. In particular, temporal means of a few OA products that incorporated other ocean measurements besides Argo show a global-scale cooling difference, which is likely related to the baseline climatology fields used to generate those products. Large differences also appear in the interannual variability in the Southern Ocean and in the long-term trends in the subpolar North Atlantic. These differences remind us of the possibility of product-dependent conclusions on OHC variations. Caution is therefore warranted when using merely one OA product to conduct OHC studies, particularly in regions and on timescales that display significant differences.

Accepted for publication in *Journal of Climate*. DOI10.1175/JCLI-D-20-0794.1.

1 Introduction

Over the past decades, about 93% of the accumulated energy imbalance of the earth system is stored in the ocean (e.g., Roemmich et al. 2015; Riser et al. 2016). Therefore, besides being one of the most important indicators of climate change, ocean heat content (OHC) provides essential constraints for estimating the global energy imbalance (Hansen et al. 2011; Trenberth et al. 2014; von Schuckmann et al. 2016; von Schuckmann et al. 2020). Many efforts have been made to unveil and understand the variability of global and regional OHC on various timescales. For the global ocean, previous studies show that OHC variations are strongly modulated by both anthropogenic forcing and natural climate variability (e.g., Lyman et al. 2010; Balmaseda et al. 2013; Xie et al. 2015). In particular, the globally integrated OHC in the upper 300 m clearly responds to major El Niño–Southern Oscillation (ENSO) events (e.g., Domingues et al. 2008; Cheng et al. 2019). Below 300 m, the globally integrated OHC is less affected by temporal variability and shows clear trends. Regionally, OHC is heavily affected by lateral and vertical redistributions and displays different variability and change (e.g., Trenberth and Fasullo, 2013; Chen and Tung, 2014; von Schuckmann et al. 2016; Liang et al. 2017).

Many previous studies on OHC variations are based on different types of ocean products, including objective analyses (OA), reanalyses and state estimates (Balmaseda et al. 2013; Chen and Tung 2014; Cheng et al. 2015, Wunsch and Heimbach, 2014). However, substantial uncertainties in various data products have been noted (e.g., Palmer et al., 2017; Wang et al. 2018). A major source of the uncertainties is the temporally and spatially sparse historical observations of ocean temperature (Desbruyères et al. 2014). The situation has been dramatically improved with the deployment of the global Argo float array since the 2000s. The Argo program, which has become a major component of the present global ocean observing system, provided

Accepted for publication in *Journal of Climate*. DOI10.1175/JCLI-D-20-0794.1.

most of the present global-scale temperature and salinity measurements in the upper 2000 m (Roemmich et al. 2009, 2015, 2019).

Several groups have used the measurements from the Argo floats to produce gridded OA products (e.g., Hosoda et al. 2008; Roemmich and Gilson, 2009; Good et al. 2013; Li et al. 2017). These products have been widely used by the oceanography and climate communities to address various ocean and climate questions (e.g., Cheng et al. 2015; Desbruyères et al. 2017). For example, previous OHC studies based on those products have revealed robust and rapid warming in the global ocean and provide constraints for estimating the Earth's energy imbalance (e.g., Trenberth et al. 2016). Despite the fact that the Argo program provides the most abundant global-scale temperature and salinity measurements over the past 15 years, apparent differences among those products that are solely or primarily based on Argo products still exist (e.g., Trenberth et al. 2016; Wang et al. 2017; Liu et al. 2020). These differences were generally attributed to the different baseline climatology and mapping methods used to produce those data products (Abraham et al. 2013; Cheng and Zhu, 2014, 2015; Boyer et al. 2016). However, as far as we are aware, a detailed examination of the differences in OHC among those OA products over the Argo period is still lacking.

In this study, following Liu et al. (2020), a companion paper focusing on the salinity field, we examine the OHC variations during the Argo period (2005-2019) from a set of widely used OA products. In contrast to previous studies, we explicitly present and examine the differences among the selected OAs. The results, particularly the differences among the examined OAs, can serve as a useful reference for future OHC studies. The paper is organized as follows: the selected OAs and the comparison methods are described in Section 2. A thorough intercomparison of the spatial and temporal variations of the global OHC from the selected OA

Accepted for publication in *Journal of Climate*. DOI10.1175/JCLI-D-20-0794.1.

products during the Argo period (2005-2019) is presented in Sections 3, 4 and 5. The results are summarized and discussed in Section 6.

2 Data and Methods

2.1 Gridded Temperature Datasets

Eight coarse resolution OA products were used in this study, including BOA global ocean Argo gridded dataset (BOA; Li et al. 2017), the Institute of Atmospheric Physics ocean gridded product (IAP; Cheng and Zhu, 2016), the Met Office EN4.2.1 (EN4; Good et al. 2013), gridded product from the International Pacific Research Center (IPRC), objective analyses from Meteorological Research Institute (Ishii; Ishii et al. 2017), MOAA-GPV from JAMSTEC (MOAA; Hosoda et al. 2008), Roemmich-Gilson Argo Climatology from the Scripps Institution of Oceanography (SIO; Roemmich and Gilson, 2009), and gridded product from National Centers for Environmental Information (NCEI; Boyer et al. 2005; Levitus et al. 2012). Most of the intercomparison conducted in this study is based on these eight coarse resolution OAs.

Seven of the OAs provide monthly gridded fields; one (the NCEI product) supplies only 3-month averages. All have the same horizontal gridding of 1°x1°. Some of the selected products include other data sources, such as expendable bathythermograph (XBT) data and CTD data (Table 1). Consequently, some of them (i.e., EN4, IAP, Ishii and NCEI) have much longer temporal coverages than the purely Argo-based products. Although the depth range varies among the selected products, all of them cover the upper 2000 m of the global ocean, where Argo floats are the primary data source. Another main difference among the OAs stems from their various interpolation techniques (e.g., Stammer et al., 2020). More specifically, EN4, MOAA and SIO used objective analysis with different covariance functions and decorrelation radii; BOA further applied a refined Barnes successive method to improve its monthly data; Ishii and NCEI used bin

Accepted for publication in *Journal of Climate*. DOI10.1175/JCLI-D-20-0794.1.

weighted averages; and IAP used an ensemble optimal interpolation method combined with model simulations to provide first-guess climatology. Some detailed information about the selected OA products is summarize in Table 1.

Two relatively high-resolution (¼°) OA climatologies, the World Ocean Atlas 2018 (WOA18) and the WOCE Argo-based ocean global climatology (WOCE Argo, Gouretski, 2018), were also used in this study. Both WOA18 and WOCE Argo cover pre-Argo period and thus use other data sources besides Argo. Because of their differences in temporal (multi-decadal climatology for WOA18, monthly climatology for WOCE Argo) and spatial resolution from the other products listed above, WOA18 and WOCE Argo were not used in generating the ensembles and intercomparison but in discussing the possible impacts of product resolution. Some further information about WOA18 and WOCE Argo is also provided in Table 1.

2.2 Methods

In this study, OHC within a certain layer was defined as:

$$OHC = \int_{h_1}^{h_2} \rho C_p T(z)\, dz \qquad (1)$$

where T is the temperature profile of seawater, and ρ and C_p are the density and heat capacity computed from the temperature, salinity and pressure based on the Thermodynamic Equation of Seawater - 2010 (TEOS-10); h_1 and h_2 are the lower and upper limits of the corresponding layer. Following previous studies (e.g., Liu et al. 2020), the analyzed layers for the intercomparison are 0-300 m, 300-700 m and 700-2000 m. Since the vertical spacing is different among the examined products, our analyses focus more on the depth-averaged fields and their temporal and spatial variations.

Accepted for publication in *Journal of Climate*. DOI 10.1175/JCLI-D-20-0794.1.

Ensemble mean and ensemble spread were used to examine the robustness of features revealed in selected OA products. Due to their different temporal intervals, monthly temperature fields from the seven monthly OA products were firstly averaged to match the 3-month resolution of NCEI. The ensemble values were then generated from the eight coarse-resolution OA products for their overlapping spatial coverage (65°N to 60°S) and time span (2005 through 2019). At each grid point, the ensemble mean was calculated as the mean of the eight OA products. The ensemble spread was defined as the standard deviation of the eight products and served as an indicator of the level of "disagreement" of the corresponding values from the selected OA products. For some quantities, a ratio of spread-to-mean was also provided to further quantify the corresponding uncertainty.

In this study, we first calculated the temporal mean of OHC to present and examine its mean state in each of the three layers over the period 2005-2019. After that, the climatological annual cycle of OHC was calculated and removed from the OHC time series at each grid point. Since the focuses of this study are the low-frequency components, a yearly running-mean was also used to remove the subannual signals, which are likely non-physical in the examined OA products (Trenberth et al. 2016). The linear trend of OHC was computed with the least-squares regression, and its uncertainty was defined as twice the standard error (95% confidence), in which the reduced degrees of freedom were considered for error correction. The interannual variability was then defined as the detrended and low-pass filtered OHC time series.

3 Spatial Patterns

3.1 Time Mean

The time mean of the ensemble mean of OHC and the spread of OA products around the ensemble mean over the Argo period are shown in Figure 1. Major well-known features appear,

Accepted for publication in *Journal of Climate*. DOI10.1175/JCLI-D-20-0794.1.

such as the Pacific Warm Pool in the 0-300 m and 300-700 m layers, and the relatively warm patches in the Indian Ocean and the North Atlantic in the 700-2000 m layer. The ensemble spread can be interpreted as a quantification of the uncertainty of the ensemble mean fields. The calculated ensemble spread (Fig. 1d-f) shows that the largest uncertainties appear along the major western boundary currents (e.g., Kuroshio and Gulf Stream) and the Antarctic Circumpolar Current (ACC) in all the examined layers. For the 0-300 m layer, large ensemble spreads also appear in the tropical regions as zonal bands. The spread-to-mean ratio (Fig. 1g-i) further depicts the relative relationship of the two terms described above. For all three layers, the overall uncertainty is very small since the spread-to-mean ratio is around or below 10^{-3} at nearly every grid point except a few regions where mesoscale variability is high (10^6 J m^{-2} of the spread to 10^9 J m^{-2} of the mean).

Although its magnitude is small, it is still useful to examine sources of the ensemble spread, particularly in regions where relatively large ensemble spread appears. Differences in temporal mean OHC between each examined OA and the ensemble mean are displayed in Figure 2. Global-scale differences appear in many of the OA products. In particular, EN4 (Fig. 2g-i) shows widespread negative differences from the ensemble mean in all the three layers. Similar patterns appear in the 0-300 m layer results from IAP, Ishii and NCEI, which all have longer time spans and utilize a lot of historical observations in the pre-Argo period. As previous studies (e.g., Boyer et al. 2016; Wang et al. 2017) suggested, the uncertainty of the time mean OHC estimates is likely related to the choice of the "first guess" climatological field as well as the mapping methods used to generate the OA products. For the case of EN4, its difference is most likely due to its choice of the baseline climatology, which represents the average temperature field over a multidecadal period before Argo (Good et al. 2013). Due to the general warming trend over the

Accepted for publication in *Journal of Climate*. DOI10.1175/JCLI-D-20-0794.1.

past decades, the mean temperature during the Argo period will be higher than that for any pre-Argo period; using the pre-Argo climatology could potentially cause OHC estimates to lower values during the Argo period. Compared to the ensemble mean, the EN4 shows a difference of -0.5°C in the 0-300 m layer and -0.2°C in the deeper layers. In addition to the global-scale differences, other interesting patterns exist. For instance, IPRC displays various zonally banded structures (Fig. 2j), which are likely associated with the altimetry SSH data used to adjust regular grids; shifts of surface currents between different time periods and consequently the SSH patterns would cause such banded structure. Also, consistent with the ensemble spread (Fig. 1d-f), many of the examined OA products show noticeable differences associated with major ocean currents.

3.2 Interannual Variability

The robust and inconsistent features of interannual variability of OHC were investigated by examining the distribution of its amplitude, defined as its temporal standard deviation (Figs. 3 & 4). The strongest interannual variability is associated with the major ocean currents in all the examined layers and appears in the tropical ocean in the upper 300 m (Fig. 3a-c). The ensemble spreads of the amplitude of the interannual variability in OHC (Fig. 3d-f) display similar patterns to the amplitude of interannual variability. More specifically, large spread appears in the Kuroshio region, the Gulf Stream, and the ACC in all the examined layers. In the upper 300 m, large spread also appears in the tropical regions, such as the Eastern Tropical Pacific and the Western Tropical Atlantic Ocean. Most regions mentioned above are usually associated with high mesoscale activity (Dong et al. 2014; Thomas et al. 2016), and the way impacts of mesoscale eddies are incorporated in different products could be a reason for the large differences in those regions. In contrast to the amplitudes and spreads of the interannual

Accepted for publication in *Journal of Climate*. DOI10.1175/JCLI-D-20-0794.1.

variability in OHC, the patterns of the spread-to-mean ratio are largely different (Fig. 3g-i). While the spread-to-mean ratio of the interannual variability is mostly below 0.5 in each of examined layers, some areas with larger values do appear in the Indian sector of the Southern Ocean, particularly in the subsurface layers. Based on values of this ratio, the uncertainty of interannual variability in OHC is clearly larger than that of the time mean (Fig. 1g-i).

The plausible sources of the ensemble spread of the amplitude of interannual variability in OHC were further investigated. Figure 4 presents the differences of the amplitude of interannual OHC variability between each OA product and the ensemble mean. The most notable feature is the differences along major ocean currents. In particular, the interannual variability from BOA is about 50% stronger than the others in regions like the ACC and western boundary currents (Fig. 4b&c). EN4, IPRC and SIO also show similar patterns in the subsurface layers, but to a lesser extent. IAP, on the other hand, shows clear negative differences along the major ocean currents. Since the associated ensemble members in each group include both Argo-only and Argo-included products (see Table 1), the source of such differences is likely the interpolation method (Boyer et al. 2016) rather than bias from certain measurements. Caution is warranted when using OA products to explore the OHC interannual variability in those regions of strong currents, particularly for conclusions that depend on the magnitude of interannual variability.

3.3 Trend

The 15-year linear trends of the globally and regionally integrated OHC in different layers were calculated (Fig.5). Globally, the trend varies from 3.6 (BOA) to 4.1 (EN4) × 10^{21} J yr^{-1} in the 0-300 m layer, 1.5 (IPRC) to 2.1 (BOA) × 10^{21} J yr^{-1} in the 300-700 m layer, 3.1 (IAP) to 4.4 (EN4) × 10^{21} J yr^{-1} in the 700-2000 m (Fig. 5). These estimated trends marginally overlap within

Accepted for publication in *Journal of Climate*. DOI10.1175/JCLI-D-20-0794.1.

the uncertainty of 2σ except for EN4 in the 700-2000 m layer. All the OA products show significant warming trends in all the three layers (Fig. 5).

While the globally integrated OHC continually increases during the examined period, substantial regional differences were observed (Figs. 5&6). Figure 6 shows spatial patterns of the linear trend of OHC over 2005-2019. As numerous prior studies have found (e.g., Gille 2008, Böning et al. 2008), substantial warming appears in the Southern Ocean in all layers. For the Pacific Ocean, a clear ENSO like structure appears in the 0-300 m and 300-700 m layers, with warming in the eastern tropical Pacific and cooling in the western tropical Pacific. However, it should be noted that trends in a large portion of the region displaying ENSO like feature are not statistically significant. Also, a warming pattern dominates the 700-2000 m layer in the Pacific. For the North Atlantic, the OHC trend shows a clear dipole pattern in all three layers, with cooling in the subpolar region and warming in the subtropical region. In contrast, the South Atlantic is dominated by a warming trend, particularly in the 300-700 m and 700-2000 m layers.

The ensemble spread of the OHC trends is presented in Fig. 6d-f. Similar to the results of the time mean and interannual variability, large spreads of the OHC trend are associated with major ocean currents (i.e., Kuroshio, Gulf Stream and the ACC). The differences in OHC trend between each OA and their ensemble mean (Fig. 7) confirm again that most of the differences occur in the most mesoscale-dynamic regions in the global ocean. But, in contrast to results of the time mean and interannual variability, differences of the OHC trends show much clearer relatively short-scale features, particularly in the upper 300 m, highlighting the challenges on interpretation of regional OHC changes based on one-degree OA products.

The trends of the horizontally averaged OHC were also examined (Fig. 8a-b). Overall, the global ocean shows widespread warming trend over 2005-2019 in the entire upper 2000 m. The largest

Accepted for publication in *Journal of Climate*. DOI10.1175/JCLI-D-20-0794.1.

trend is observed within the top 50 m (around 3×10^{19} J yr^{-1}) but with large uncertainty, and then rapidly decreases to 0.5-0.7 × 10^{19} J yr^{-1} around 150 m. Below 150 m, the warming rate decreases slowly with depth in all examined products. The warming trends are overall significant except between 150-250 m where the 95% confidence interval cross zero. The trends of the zonally averaged OHC shows a number of similar patterns in all examined layers (Fig. 8c-e), such as cooling in the northern subpolar region and warming south of 30°S although some are not significantly different from zero. Combining with Figure 6, we can see that the subpolar cooling in the Northern Hemisphere comes from the Atlantic. For regions between 30°S and 30°N, the upper 300 m (Fig. 8c) shows substantial differences from the layers below. In particularly, a cooling trend appears around 10°N in the 0-300 m layer, which is very likely ENSO related, but disappears in the layers below. Again, this indicates the calculation of global OHC trend in the upper ocean will be heavily affected by ENSO events that occurred during the examined period.

Figure 8 also shows a few notable differences in the vertical and meridional structures of the long-term global OHC trends. Vertically, EN4 consistently shows stronger warming than other products; NCEI displays a small and suspicious signal around 800 m; and IPRC and SIO show similar and weaker warming between 300 m and about 1000 m. Meridionally, the most evident differences appear in the northern subpolar region (Fig. 8c-f). More specifically, IPRC, BOA, MOAA and SIO show strong cooling both in the top 300 m and below, but IAP, EN4, Ishii and NCEI show much weaker cooling or even warming trend in the northern subpolar region. Since the two groups are largely different in their data sources, i.e., with or without other measurements besides Argo, the use of other ocean measurements in the high latitude regions could be the reason for the substantial differences. Cautions should be taken when describing and

Accepted for publication in *Journal of Climate*. DOI10.1175/JCLI-D-20-0794.1.

interpreting OHC changes in regions displaying significant differences, particularly the subpolar Atlantic Ocean and subsurface ocean.

4 Temporal Patterns

4.1 Time Series

Time series of the globally integrated OHC (after removing the annual cycles) in each examined layer are presented in Figure 9. In general, temporal variations of OHC are consistent among the examined OA products. The integrated OHC in different layers show variations on different timescales, ranging from interannual variations to decadal trends. Regarding the interannual variations, ENSO is the dominant climate mode (Balmaseda et al. 2013; Trenberth et al. 2014). The warm and cold ENSO events since 2005 are marked as color bands in Figure 9. The OHC, particularly in the upper 300 m layer, generally decreases (increases) during warm (cool) ENSO events, likely related to the energy exchange at the sea surface (Trenberth et al. 2002; Mayer et al. 2014). On the decadal scale, robust warming occurs in all three layers. Our calculation shows that the 0-300 m and the 700-2000 m layer each accounts for about 40% of the OHC changes in the entire upper 2000 m, and the 300-700 m layer makes up the other 20%.

We also calculated the 5-year rolling trends of OHC in each layer following Smith et al. (2015). By doing so, we highlight the differences among the OHC variations from the selected OAs (Fig. 10). All 5-year trends in the 0-300 m layer are positive and below 9×10^{21} J yr^{-1}. For the 300-700 m and 700-2000 m layers, most of the 5-year trends are positive except a few years at the beginning and end of the examined period. The most apparent differences among the examined OA products appear in the 0-300 m layer, where much larger trends are estimated from SIO between 2013 and 2016, indicating much faster warming in SIO over that period. Further examination reveals that these differences (see Fig. 12) are mostly from the top 200 m and are

Accepted for publication in *Journal of Climate*. DOI10.1175/JCLI-D-20-0794.1.

likely due to the uncertainties related to the unusual ENSO events in the most recent decade (Kim et al. 2011; Hu and Fedorov, 2019). Better agreement is achieved for the 300-700 and 700-2000 m layers, in which the strongest five-year warming trend appears following the 2010/2011 La Niña event.

4.2 Time Evolution as Functions of Depth and Latitude

More information on temporal variations of the OHC over the global ocean can be obtained from its time evolution as a function of depth (Figs. 11 and 12) and of latitude (Figs. 13 & 14). Figure 11a presents the time evolution of vertical profiles of the horizontally integrated OHC anomaly (relative to the time means). The OHC anomaly in the upper ocean is strongly correlated with the Oceanic Niño Index, with a correlation coefficient around 0.7 in the top 100 m and -0.6 at 200 m. The opposite signs of the correlation coefficients at different depths indicate that in addition to the air-sea heat exchanges modulated by ENSO (e.g., Trenberth et al. 2005; Roemmich and Gilson 2011; Cheng et al. 2015, 2019), the vertical redistribution of heat, which is associated with the vertical movement of the thermocline, likely contributes to the upper-ocean temperature changes as well. The ocean below 300 m shows a broad warming that decreases with depth and generally has a much weaker correlation with the Oceanic Niño Index. We also examined the evolution of the spread of OHC anomaly (Fig. 11b,d), which is generally small except the beginning years of the examined period (spread-to-mean ratio around 0.5) and decreases with increasing depth. The large spread at the beginning of the Argo period is likely due to the smaller number of Argo floats.

The differences in temporal variations of the OHC profiles between each OA product and the ensemble mean are shown in Figure 12. The difference from the ensemble mean ranges about half of the mean OHC in Figure 11, and varies distinctively across the examined products. For

Accepted for publication in *Journal of Climate*. DOI10.1175/JCLI-D-20-0794.1.

instance, EN4 displays stronger temporal variations than the ensemble mean for its differences present the same pattern to the ensemble mean (cf. Fig. 11a & c and Fig. 12 e & f). On the contrary, differences of SIO present an opposite pattern to the ensemble mean and therefore likely show overall weaker temporal variability (cf. Fig. 11a & c, and Fig. 12 m & n). The other products also present small differences on interannual to decadal timescales. In particular, NCEI shows some differences around 800 m, which is warmer before 2010 and cooler after, causing the "spike" in Figure 8b. Overall, while the ENSO signal in the upper ocean and the widespread warming along the entire water column are robust, the observed differences imply that the detailed vertical structures are represented slightly differently by the different OA products, which can also be inferred from Figure 8b.

The time series of the zonally averaged OHC anomaly is shown in Figure 13. For the 0-300 m layer, the tropical region between 20°N and 20°S presents high interannual variability associated with ENSO, appearing as strong meridional redistribution of OHC. Mid-latitude Southern Hemisphere and Northern Hemisphere show clear warming, and the subpolar region of 60°N - 65°N displays substantial cooling. In the deeper layers, except for a significant cooling trend in the northernmost region, the variation of the zonally averaged OHC is dominated by long-term warming with different strength. The spread of the zonally averaged OHC (Fig. 13d-f) shows that the most substantial difference appears in the high latitude region in the Northern Hemisphere. More specifically, as shown in the differences between each OA product and the ensemble mean (Fig. 14), the cooling in the northern subpolar region is weaker in at least five of the eight examined OAs (i.e., IAP, EN4, Ishii, MOAA and NCEI) than results from the ensemble mean; each of these OA products incorporates other ocean measurements besides Argo data. In

Accepted for publication in *Journal of Climate*. DOI10.1175/JCLI-D-20-0794.1.

addition, a number of differences on interannual timescales appear in different regions of the various OA products, mostly poleward of 30°S and 30°N.

5 Spatial-Temporal Modes

To reveal the possible differences in interpreting OHC variations from different OA products, a common EOF analysis was applied to each OA product and their ensemble mean to identify and compare their major spatial-temporal modes. Figure 15 shows the first two EOF modes in each of the examined layers based on the ensemble of the selected OA products. For the upper 300 m, the leading mode shows an ENSO-related pattern in the Pacific Ocean and a dipole pattern in the North Atlantic (Fig. 15a). The second mode shows some banded structures in the Pacific and a dipole in the North Atlantic but with different polarities from the first mode (Fig. 15d). For the 300-700 m layer, its first EOF mode displays similar but nosier patterns to the first mode of the 0-300 m layer, suggesting this layer is affected by similar dynamics as the top layer. For the 700-2000 m layer, the first mode displays uniform change in most regions of the global ocean except the North Atlantic and the Southern Ocean. The second mode also shows various basin-scale changes, but their spatial patterns are nosier than the first mode.

The normalized EOF patterns from each of the examined OAs are presented in Figures 16&17. In general, the EOF patterns are more consistent in the top layer than in the deep layers, and the first mode is more consistent than the second and other higher modes. For instance, the first EOF mode (Fig. 16) in the 0-300 m layer from all the products shows almost identical large-scale spatial patterns despite the different percentage of explained variance. Although their agreement is not as striking as in the 0-300 m, reasonable consistency in large-scale structures is also achieved for the first EOF mode of the 300-700 m and 700-2000 m layers. The structures of the second mode show more differences than the first mode does (Fig. 17). In particular, the zonal

Accepted for publication in *Journal of Climate*. DOI10.1175/JCLI-D-20-0794.1.

banded structure in the Pacific Ocean and the dipole pattern in the North Atlantic in the 0-300 layer are much weaker in EN4 than in other OAs. In addition, many relatively small-scale patterns appear in BOA but not that clear in the other OA products.

The PCs of the leading EOF modes (Fig. 18) are usually used to detect major modes of climate variability (e.g., Chen and Tung, 2014). For instance, in the 0-300 m layer, PC1 is correlated with the Oceanic Niño Index at relatively high rates around 0.80. In deeper layers, PCs show long-term change in the first mode, and decadal oscillation in the second mode. Although the EOF patterns in general agree well among the examined OA products, particularly in the 0-300 m layer, noticeable differences are found in the PCs. More specifically, although the PC1 values agree well in the 0-300 layer, the PC2 values have considerably larger spread, with the results from EN4 the most noticeable. SIO has a positive signal in PC2 between 2016 and 2017, while the others are either negative or close to zero.

In the 300-700 m layer, all PC1 values indicate a trend. However, the trend from BOA is significantly larger (more negative at beginning of record and more positive at the end). PC1 from SIO generally agrees with the values from other OA products at the beginning of the record but is substantially higher at the end, although not as much as that from the BOA product. The PC2 from BOA is also a clear in the 300-700m layer. All products have similar PCs for the deepest layer considered. The differences revealed here could potentially lead to different interpretation on the strength of the observed climate variability depending on the product used, especially for the 300-700 m layer.

6 Summary and Discussion

In this study, we compared the global OHC variations from eight widely used OA products with a focus on their robust features as well as differences over the Argo period, when Argo

Accepted for publication in *Journal of Climate*. DOI10.1175/JCLI-D-20-0794.1.

measurements serve as their only or major data source. Our intercomparison confirmed that widespread warming occurred in the upper 2000 m of the global ocean and the largest warming rate appeared in the top 150 m (Figs. 8&9). Robust spatial patterns of the OHC changes in all examined layers were also obtained. In particular, as many prior studies have shown (e.g., Roemmich et al. 2015; von Schuckmann et al. 2020), the Southern Ocean and mid-latitude North Atlantic have experienced substantial warming, and the subpolar North Atlantic shows an apparent cooling (Figs. 6&8).

In comparison to a similar study on ocean salinity (Liu et al. 2020), the overall differences in OHC across the examined OA products are not as marked as in the salinity products. With that said, a few substantial differences were still identified on various timescales and in different regions (e.g., major ocean currents). By examining their spatial patterns, we found that a few OA products that incorporated measurements other than Argo and had longer time span (e.g., EN4) display global-scale differences of negative sign from the others in the temporal mean, particularly in the 0-300 m layer (Fig. 2). As previous studies (e.g., Boyer et al. 2016; Wang et al. 2017) have suggested, these differences are likely related to the choice of the climatological field that were used to generate the OA products. On the interannual timescale, substantial differences appear in regions with strong interannual variability, such as near major ocean currents (Fig. 4). In particular, BOA disagrees significantly from the others in the Southern Ocean and North Atlantic in the 0-300 m layer. On the long-term trend, while the global and regional OHC trends are consistent among the OAs, there are also some noticeable exceptions like the patch in the tropical Atlantic in the 700-2000 m layer from IAP (Fig. 6), the different magnitude of warming between 300 and 2000 m, and the divergent cooling magnitude in the subpolar northern latitudes (Fig. 8).

Accepted for publication in *Journal of Climate*. DOI10.1175/JCLI-D-20-0794.1.

By examining the spatial and temporal structure of OHC variations, we were able to provide more information on when and where these differences happened. Vertically, EN4 shows higher-than-average trends at all depth, and NCEI shows a suspicious trend at 800 m depth (Fig. 8). For the other OAs, small differences are also observed on interannual to decadal timescales. Zonally, most examined OAs (i.e., IAP, EN4, Ishii, MOAA and NCEI) show a weaker cooling in the northern subpolar regions than the ensemble (Fig. 14), indicating the OAs solely based on Argo floats, which are not so abundant in the subpolar latitudes, could overestimate the warming in that region. Through a common EOF analysis, we found that the leading modes of the OAs are largely similar on the spatial patterns and PCs. While the 0-300 m layer is clearly under impact of ENSO, the deeper layers show long-term trend in mode 1 and decadal oscillation in mode 2. Nevertheless, noticeable differences were also identified, and these differences are more likely coming from OAs with longer time span, which could make it harder for them to adjust the warming acceleration correctly.

It is worth noting that the patterns of ensemble spreads of the time mean, interannual variability and long-term trend are all closed related to the most dynamic regions in the ocean, where mesoscale eddies are abundant (Figs. 1, 3&6). The most substantial differences appearing in those regions suggest that the selected OA products are limited by the relatively sparse data or their low resolutions, which are inadequate to resolve the mesoscale structures (e.g., Seidov et al. 2019). As a preliminary test of the possible impacts of higher grid resolution, we compared the temporal mean from the one-degree ensemble mean with two currently available ¼ degree OA products, WOA and WOCE-Argo Climatology, both of which were subsampled at the same one-degree grids as the other OAs (Fig. 19). Both high resolution products show good agreement with the ensemble mean, but noticeable differences still appear along the major ocean current

Accepted for publication in *Journal of Climate*. DOI10.1175/JCLI-D-20-0794.1.

systems, particularly in the 300-700 m layer. This test indicates that although increased OA resolutions could help, ultimately denser in-situ observations are needed to reduce the differences in those dynamic regions.

The existence of various differences in OHC among the examined OA products during the most data abundant Argo period suggests the possibility of product-dependent conclusions, particularly for studies in regions and on timescales that display substantial differences. Caution is therefore warranted before making any strong conclusions if only one OA data has been examined. Also, similar to our previous finding on the ocean salinity, which is based on some of the OA products used here (Liu et al. 2020), while the number of Argo floats has increased stably since 2005 (Johnson et al. 2015; Wijffels et al. 2016; Riser et al. 2016; Boyer et al. 2018), regional differences (e.g., Figs. 3 and 6) still exist in some of the most dynamic regions (e.g., the Southern Ocean and the western boundary currents). This work highlights the necessity of denser in-situ observations in those dynamic regions as well as OA products of higher-resolution, which are and will be essential for addressing various ocean and climate questions.

Acknowledgments

The authors thank three anonymous reviewers for their helpful comments and suggestions. The work was supported in part by the National Science Foundation through Grant OCE-2021274 and the National Aeronautics and Space Administration through Grant 80NSSC20K0752 and 80NSSC20K0728. All the data used in this study are publicly available. BOA (ftp://data.argo.org.cn/pub/ARGO/BOA_Argo/); IAP (http://159.226.119.60/cheng/); EN4 (https://www.metoffice.gov.uk/hadobs/en4/index.html); IPRC

Accepted for publication in *Journal of Climate*. DOI10.1175/JCLI-D-20-0794.1.

(http://apdrc.soest.hawaii.edu/projects/Argo/); Ishii (https://climate.mri-jma.go.jp/pub/ocean/ts/v7.3/); MOAA (http://www.godac.jamstec.go.jp/argogpv/); SIO (http://sio-argo.ucsd.edu/RG_Climatology.html); NCEI (https://www.ncei.noaa.gov/access/global-ocean-heat-content/); WOA18 (https://www.ncei.noaa.gov/products/world-ocean-atlas); WOCE-Argo (https://doi.org/10.1594/WDCC/WAGHC_V1.0).

References

Abraham, J. P. et al. 2013: A review of global ocean temperature observations: Implications for ocean heat content estimates and climate change, *Rev. Geophys.* 51, 450– 483, https://doi.org/10.1002/rog.20022.

Balmaseda M.A. K.E. Trenberth, E Kaellen, 2013: Distinctive climate signals in reanalysis of global ocean heat content. *Geophys Res Lett* 40:1754–1759, https://doi.org/10.1002/grl.50382

Boyer, T. P., S. Levitus, J. I. Antonov, R. A. Locarnini, and H. E. Garcia, 2005: Linear trends in salinity for the World Ocean, 1955–1998. *Geophys. Res. Lett.,* **32**, L01604, https://doi.org/10.1029/2004GL021791.

Böning, C., Dispert, A., Visbeck, M. *et al.* 2008: The response of the Antarctic Circumpolar Current to recent climate change. *Nature Geosci* **1,** 864–869. https://doi.org/10.1038/ngeo362

Boyer, T. et al. 2016: Sensitivity of Global Upper-Ocean Heat Content Estimates to Mapping Methods, XBT Bias Corrections, and Baseline Climatologies. *J. Climate,* **29**, 4817–4842, https://doi.org/10.1175/JCLI-D-15-0801.1.

Accepted for publication in *Journal of Climate*. DOI10.1175/JCLI-D-20-0794.1.

Boyer, T.P. et al. 2018: World Ocean Database 2018. A. Mishonov, technical ed. *NOAA Atlas NESDIS 87*, https://data.nodc.noaa.gov/woa/WOD/DOC/wod_intro.pdf.

Chen X, K.K. Tung, 2014: Varying planetary heat sink led to global warming slowdown and acceleration. *Science* 345:897–903. https://doi.org/10.1126/science.1254937

Cheng L, F Zheng, J Zhu, 2015: Distinctive ocean interior changes during the recent warming slowdown. *Sci Rep*. https://doi.org/10.1038/srep14346

Cheng, L., and J. Zhu 2014: Artifacts in variations of ocean heat content induced by the observation system changes, *Geophys. Res. Lett*., 41, 7276–7283, https://doi.org/10.1002/2014GL061881

Cheng, L., and J. Zhu, 2015: Influences of the Choice of Climatology on Ocean Heat Content Estimation. *J. Atmos. Oceanic Technol.*, **32**, 388–394, https://doi.org/10.1175/JTECH-D-14-00169.1.

Cheng, L., and J. Zhu, 2016: Benefits of CMIP5 multimodel ensemble in reconstructing historical ocean subsurface temperature variation. *J. Climate*, **29**, 5393–5416, https://doi.org/10.1175/JCLI-D-15-0730.1.

Cheng, L. K. E. Trenberth, J. T. Fasullo, M. Mayer, M. Balmaseda, and J. Zhu, 2019: Evolution of Ocean Heat Content Related to ENSO. *J. Climate*, **32**, 3529–3556, https://doi.org/10.1175/JCLI-D-18-0607.1.

Desbruyères DG et al. 2014: Full-depth temperature trends in the northeastern Atlantic through the early 21st century. *Geophys Res Lett* 41:7971–7979. https://doi.org/10.1002/2014GL061844

Desbruyères, D., E. L. McDonagh, B. A. King, and V. Thierry, 2017: Global and Full-Depth Ocean Temperature Trends during the Early Twenty-First Century from Argo and Repeat Hydrography. *J. Climate*, **30**, 1985–1997, https://doi.org/10.1175/JCLI-D-16-0396.1.

Domingues, C. Church, J. White, N. Gleckler, P. Wijffels, S. Barker, P. and Dunn, J. 2008: Improved estimates of upper-ocean warming and multi-decadal sea-level rise. *Nature*, *453*(7198), 1090-1093, https://doi.org/10.1175/2010jtecho773.1.

Dong, C. J. C. McWilliams, Y. Liu, and D. Chen, 2014: Global heat and salt transports by eddy movement, *Nat Commun, 5*, 3294, https://doi.org/10.1038/ncomms4294.

Gille, S. T. 2008: Decadal-Scale Temperature Trends in the Southern Hemisphere Ocean, *Journal of Climate*, *21*(18), 4749-4765. https://doi.org/10.1175/2008JCLI2131.1.

Good, S. A. M. J. Martin, and N. A. Rayner, 2013: EN4: Quality controlled ocean temperature and salinity profiles and monthly objective analyses with uncertainty estimates, *J. Geophys. Res. Oceans, 118*(12), 6704.6716, https://doi.org/10.1002/2013jc009067.

Gouretski, V. 2018: World Ocean Circulation Experiment-Argo Global Hydrographic Climatology. *Ocean Science*, 14(5), 1127–1146, https://doi.org/10.5194/os-14-1127-2018.

Hansen, J. M. Sato, P. Kharecha, and K. von Schuckmann, 2011: Earth's energy imbalance and implications. *Atmos. Chem. Phys*. 11, 13 421–13 449, https://doi.org/10.5194/acp-11-13421-2011

Hosoda, S. Ohira, T. and Nakamura, T. 2008: A monthly mean dataset of global oceanic temperature and salinity derived from Argo float observations. *JAMSTEC Report of Research and Development, 8,* 47-59.

Accepted for publication in *Journal of Climate*. DOI10.1175/JCLI-D-20-0794.1.

Hu, S. Fedorov, A.V. 2019: The extreme El Niño of 2015–2016: the role of westerly and easterly wind bursts, and preconditioning by the failed 2014 event. *Clim Dyn* **52,** 7339–7357, https://doi.org/10.1007/s00382-017-3531-2.

Johnson G.C, J.M. Lyman, S.G. Purkey, 2015: Informing deep Argo array design using Argo and full-depth hydrographic section data, *J. Atmos. Ocean Technol. 32,* 2187–2198. https://doi.org/10.1175/JTECH-D-15-0139.1.

Kim, W. Yeh, S.- W. Kim, J.- H. Kug, J.- S. and Kwon, M. 2011: The unique 2009–2010 El Niño event: A fast phase transition of warm pool El Niño to La Niña, *Geophys. Res. Lett.* 38, L15809, . https://doi.org/10.1029/2011GL048521.

Levitus, S., and Coauthors, 2012: World ocean heat content and thermosteric sea level change (0–2000 m), 1955–2010. *Geophys. Res. Lett.,* **39**, L10603, https://doi.org/10.1029/2012GL051106.

Li, H. F. H. Xu, W. Zhou, D. X. Wang, J. S. Wright, Z. H. Liu, and Y. L. Lin, 2017: Development of a global gridded Argo data set with Barnes successive corrections, *J. Geophys. Res. Oceans, 122*(2), 866-889, https://doi.org/10.1002/2016jc012285.

Liang, X., C. G. Piecuch, R. M. Ponte, G. Forget, C. Wunsch, and P. Heimbach, 2017: Change of the global ocean vertical heat transport over 1993–2010. *J. Climate,* 30, 5319–5327, https://doi.org/10.1175/JCLI-D-16-0569.1

Liu, C. X. Liang, D. P. Chambers, and R. M. Ponte, 2020: Global Patterns of Spatial and Temporal Variability in Salinity from Multiple Gridded Argo Products. *J. Climate*,1-42, https://doi.org/10.1175/JCLI-D-20-0053.1.

Accepted for publication in *Journal of Climate*. DOI10.1175/JCLI-D-20-0794.1.

Ishii, M., Y. Fukuda, S. Hirahara, S. Yasui, T. Suzuki, and K. Sato, 2017: Accuracy of global upper ocean heat content estimation expected from present observational data sets. *SOLA*, **13**, 163–167, https://doi.org/10.2151/SOLA.2017-030.

Lyman, J. Good, S. Gouretski, V. *et al.* 2010: Robust warming of the global upper ocean. *Nature* **465,** 334–337. https://doi.org/10.1038/nature09043

Mayer, M. L. Haimberger, and M. A. Balmaseda, 2014: On the Energy Exchange between Tropical Ocean Basins Related to ENSO. *J. Climate*, **27**, 6393–6403, https://doi.org/10.1175/JCLI-D-14-00123.1.

Riser SC, Freeland HJ, Roemmich D et al, 2016: Fifteen years of ocean observations with the global Argo array, *Nat. Clim. Change, 6,* 145–153. https://doi.org/10.1038/nclimate2872.

Roemmich, D. and J. Gilson, 2009: The 2004.2008 mean and annual cycle of temperature, salinity, and steric height in the global ocean from the Argo Program, *Prog. Oceanogr. 82*(2), 81.100, https://doi.org/10.1016/j.pocean.2009.03.004.

Roemmich, D. and J. Gilson, 2011: The global ocean imprint of ENSO. *Geophys. Res. Lett.* 38, L13606, https://doi.org/10.1029/2011GL047992.

Roemmich, D. et al. 2009: The Argo Program Observing the Global Ocean with Profiling Floats, *Oceanography, 22*(2), 34.43, https://doi.org/10.3389/fmars.2019.00439.

Roemmich, D., J. Church, J. Gilson, D. Monselesan, P. Sutton, and S. Wijffels, 2015: Unabated planetary warming and its ocean structure since 2006. *Nat. Climate Change,* 5, 240–245, https://doi.org/10.1038/nclimate2513.

Accepted for publication in *Journal of Climate*. DOI10.1175/JCLI-D-20-0794.1.

Seidov, D., Mishonov, A., Reagan, J., & Parsons, R. 2019: Eddy- resolving in situ ocean climatologies of temperature and salinity in the Northwest Atlantic Ocean. *J. Geophys. Res. Oceans*, 124, 41– 58. https://doi.org/10.1029/2018JC014548.

Smith, D. M., Allan, R. P., Coward, A. C., Eade, R., Hyder, P., Liu, C., Loeb, N. G., Palmer, M. D., Roberts, C. D. and Scaife, A. A. 2015: Earth's energy imbalance since 1960 in observations and CMIP5 models. *Geophys. Res. Lett.*, 42: 1205– 1213. https://doi.org/10.1002/2014GL062669.

Stammer, D., Martins, M. S., Köhler, J., & Köhl, A., 2021: How well do we know ocean salinity and its changes?. *Progress in Oceanography*, 190, 102478. https://doi.org/10.1016/j.pocean.2020.102478.

Thomas, L. N. J. R. Taylor, E. A. D'Asaro, C. M. Lee, J. M. Klymak, and A. Shcherbina, 2016: Symmetric Instability, Inertial Oscillations, and Turbulence at the Gulf Stream Front. *J. Phys. Oceanogr.* **46**, 197–217, https://doi.org/10.1175/JPO-D-15-0008.1.

Trenberth, K. E. J. M.Caron, D. P.Stepaniak, and S.Worley, 2002: Evolution of El Niño–Southern Oscillation and global atmospheric surface temperatures. *J. Geophys. Res*. 107, 4065,https://doi.org/10.1029/2000JD000298.

Trenberth, K.E. D. P. Stepaniak, and L. Smith, 2005: Interannual variability of patterns of atmospheric mass distribution. *J. Climate,* 18, 2812–2825, https://doi.org/10.1175/JCLI3333.1.

Trenberth, K. E. J. T. Fasullo, 2013: An apparent hiatus in global warming? *Earths Future* 1:19–32. https://doi.org/10.1002/2013EF000165.

Accepted for publication in *Journal of Climate*. DOI10.1175/JCLI-D-20-0794.1.

Trenberth, K. E. J. T. Fasullo, and M. A. Balmaseda, 2014: Earth's Energy Imbalance. *J. Climate*, **27**, 3129–3144, https://doi.org/10.1175/JCLI-D-13-00294.1.

Trenberth, K.E. J.T. Fasullo, K. von Schuckmann, and L. Cheng, 2016: Insights into Earth's Energy Imbalance from Multiple Sources. *J. Climate, 29*, 7495–7505, https://doi.org/10.1175/JCLI-D-16-0339.1.

Von Schuckmann et al. 2016: An imperative to monitor Earth's energy imbalance. *Nat. Climate Change*, 6, 138–144, https://doi.org/10.1038/nclimate2876.

Von Schuckmann, K., Cheng, L., Palmer, M.D., Hansen, J., Tassone, C., Aich, V., Adusumilli, S., Beltrami, H., Boyer, T., Cuesta-Valero, F.J. and Desbruyères, D., 2020: Heat stored in the Earth system: where does the energy go?. *Earth System Science Data*, 12(3), 2013-2041.

Wang, G. J. L. J. Cheng, T. Boyer, and C. Y. Li, 2017: Halosteric Sea Level Changes during the Argo Era, *Water*, *9*(7), 484, https://doi.org/10.3390/w9070484.

Wang, G. Cheng, L. Abraham, J. & Li, C. 2018: Consensuses and discrepancies of basin-scale ocean heat content changes in different ocean analyses. *Clim. Dyn. 50*(7-8), 2471-2487, https://doi.org/10.1007/s00382-017-3751-5.

Wijffels S, Roemmich D, Monselesan D et al. 2016: Ocean temperatures chronicle the ongoing warming of Earth, *Nat. Clim. Change, 6,* 116–118. https://doi.org/10.1038/nclimate2924.

Wunsch, C. and Heimbach, P., 2014. Bidecadal thermal changes in the abyssal ocean. *J. Phys. Oceanogr.* 44(8), 2013-2030. https://doi.org/10.1175/JPO-D-13-096.1

Xie SP, Yu K, Okumura YM , 2015: Distinct energy budgets for anthropogenic and natural changes during global warming hiatus. *Nat Geosci*. https://doi.org/10.1038/NGEO2581

Accepted for publication in *Journal of Climate*. DOI10.1175/JCLI-D-20-0794.1.

Table 1 Overview of the OA products used in this study. Data with ¼ degree resolution are in italics; the others are with 1 degree resolution.

Product	Spatial Coverage	Temporal Coverage	Vertical Resolution	Data Source	Interpolation Method	References
BOA	80S-80N	2004-present	58 levels to 1975 m	Argo only	Barnes Successive Method	Li et al. 2017
IAP	90S-90N	1940-present	41 levels to 2000 m	Argo plus others	Ensemble Optimum Interpolation	Cheng and Zhu, 2016
EN4	90S-90N	1900-present	42 levels to 5350 m	Argo plus others	Objective Analysis	Good et al. 2013
IPRC	63S-63N	2005-present	27 levels to 2000 m	Argo plus Altimetry	Variational Analysis Technique	http://apdrc.soest.hawaii.edu/projects/argo/
Ishii	90S-90N	1955-present	28 levels to 3000 m	Argo plus others	Bin-Average	Ishii et al. 2017
MOAA	60S-70N	2001-present	25 levels to 2000 m	Argo plus others	Objective Analysis	Hosoda et al. 2008
SIO	64S-80N	2004-present	58 levels to 2000 m	Argo only	Weighted Least-Squares Fit	Roemmich and Gilson, 2009
NCEI	90S-90N	1955-present	26 levels to 2000 m	Argo plus others	Bin-Average	Levitus et al. 2012
WOA18	*90S-90N*	*2005-2017*	*102 levels to 5500 m*	*Argo plus others*	*Bin-Average*	*Boyer et al. 2005*
WOCE-Argo	*80S-90N*	*1985-2016*	*65 levels to 6650 m*	*Argo plus others*	*Optimal Interpolation*	*Gouretski, 2018*

Accepted for publication in *Journal of Climate*. DOI10.1175/JCLI-D-20-0794.1.

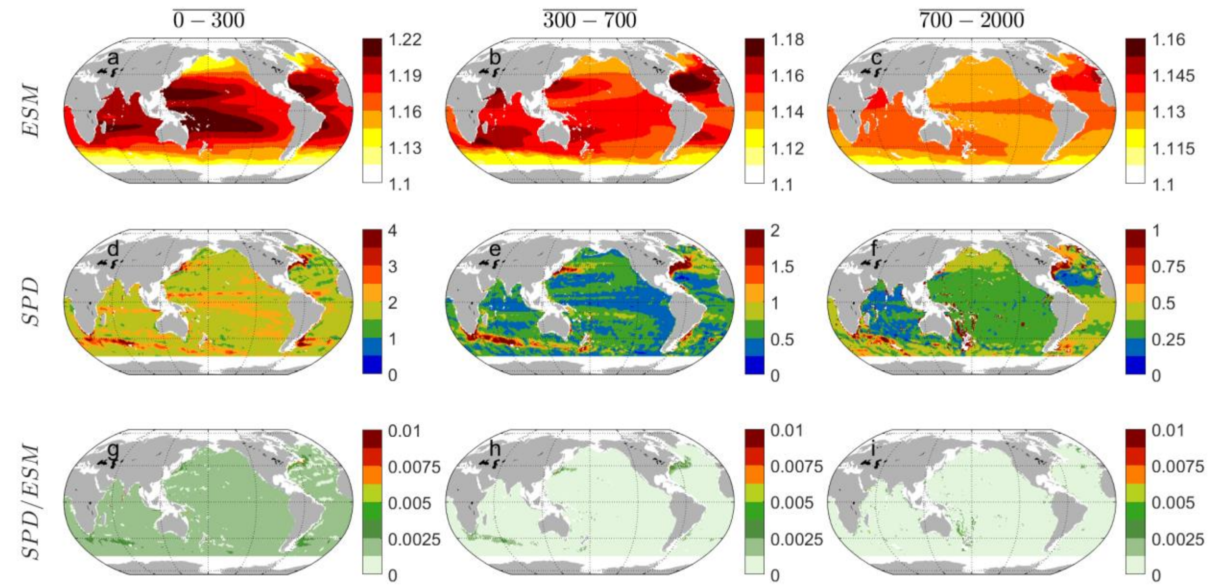

Fig. 1 Ensemble mean (ESM), ensemble spread (SPD), and the spread/mean ratio (SPD/ESM) of the time mean of depth-averaged OHC for the period 2005-2019. (Unit: 10^9 J m^{-2} for the ensemble mean, 10^6 J m^{-2} for ensemble spread)

Accepted for publication in *Journal of Climate*. DOI10.1175/JCLI-D-20-0794.1.

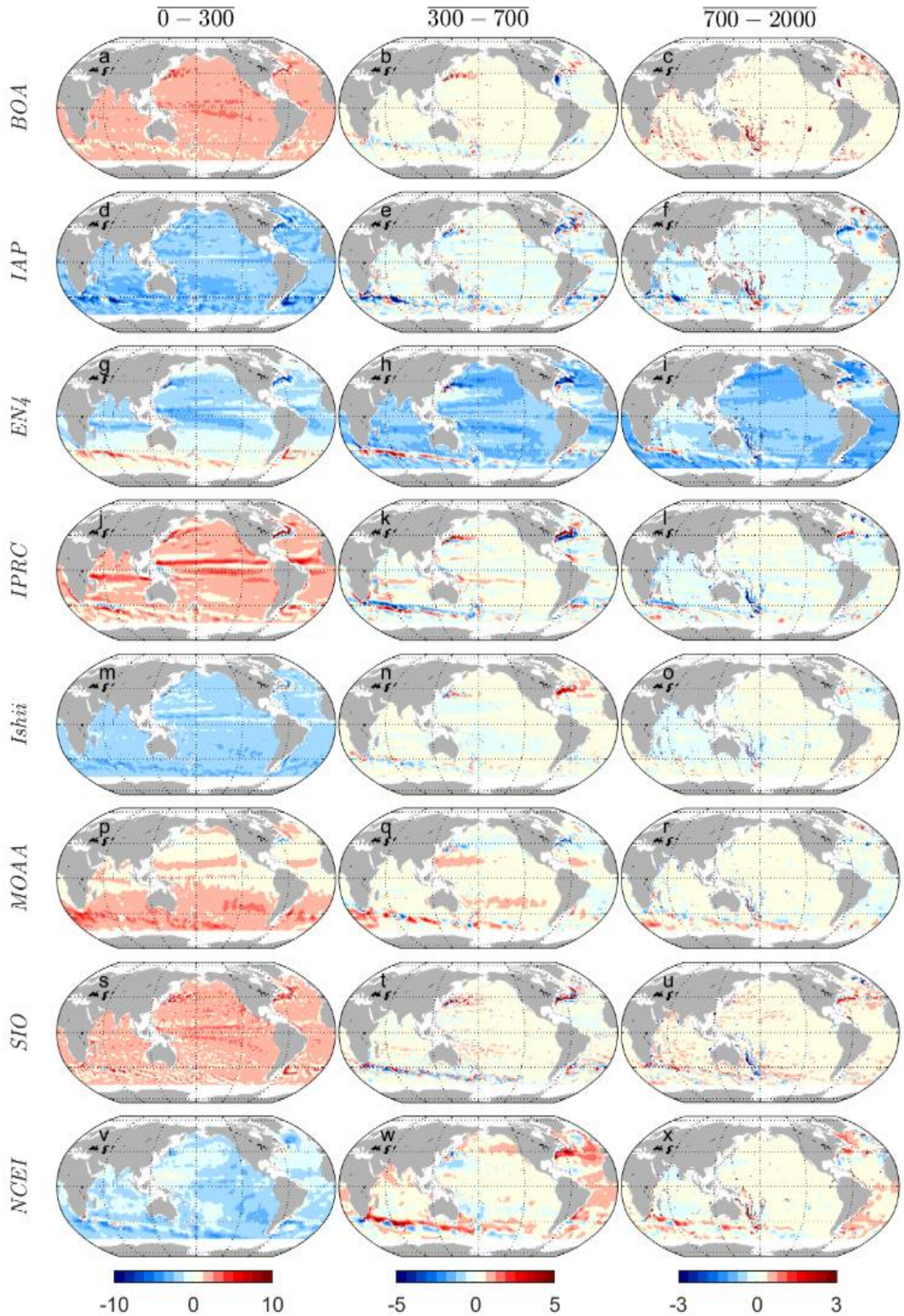

Fig. 2 Difference of time means of depth-averaged OHC between each product and the ensemble mean. (Unit: 10^6 J m^{-2})

Accepted for publication in *Journal of Climate*. DOI10.1175/JCLI-D-20-0794.1.

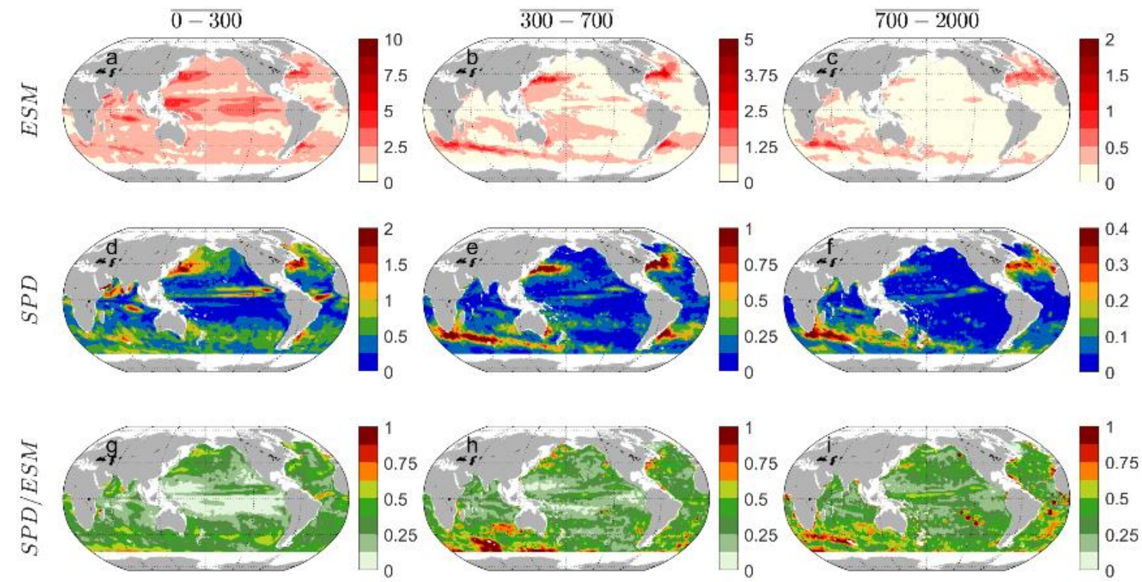

Fig. 3 Ensemble mean (ESM), ensemble spread (SPD), and the spread/mean ratio (SPD/ESM) of the amplitude of interannual variability in the depth-averaged OHC for the period 2005-2019. For panels a-f, the unit is 10^6 J m^{-2}.

Accepted for publication in *Journal of Climate*. DOI10.1175/JCLI-D-20-0794.1.

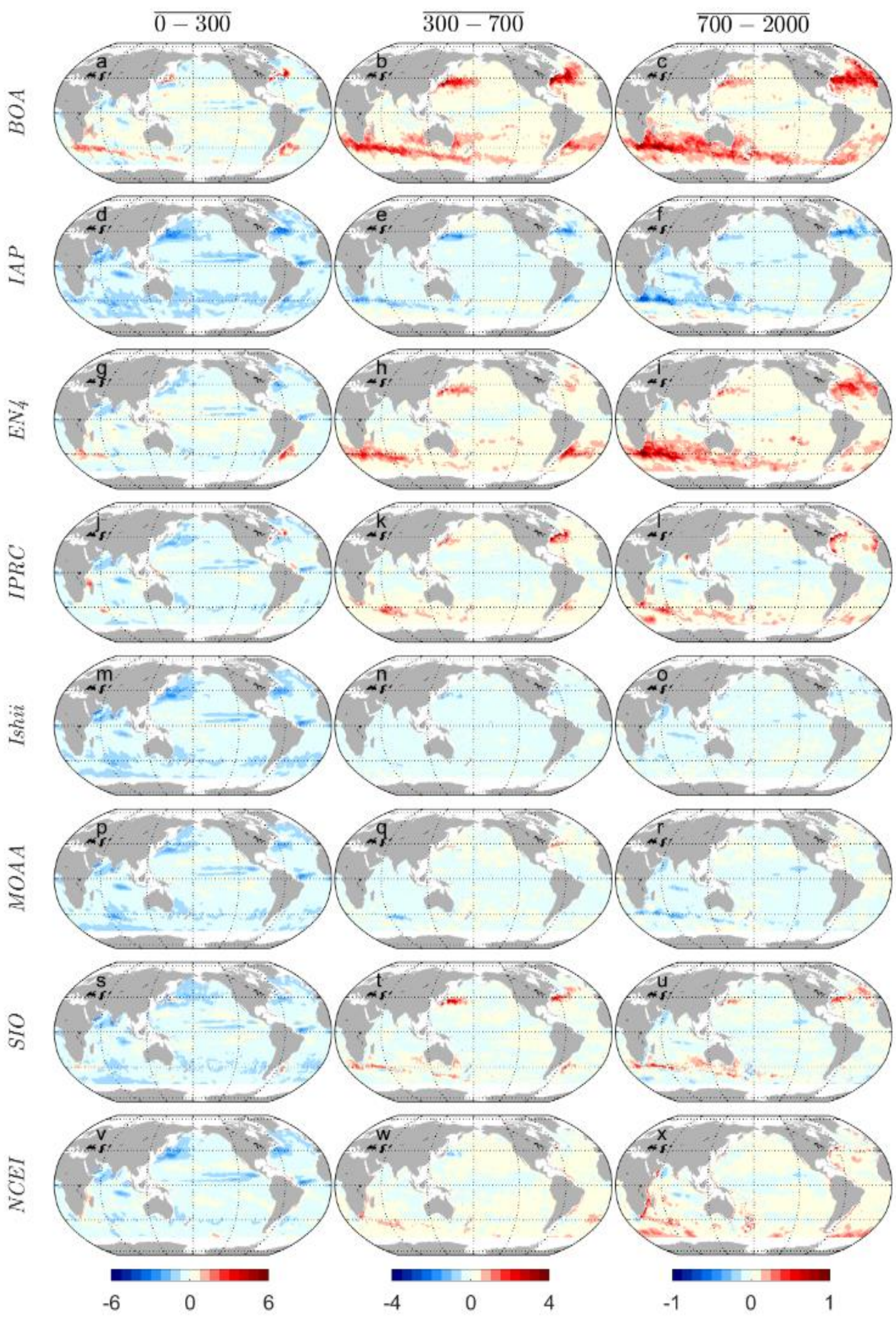

Fig. 4 Difference of interannual variability of depth-averaged OHC between each product and the ensemble mean. (Unit: 10^6 J m^{-2})

Accepted for publication in *Journal of Climate*. DOI10.1175/JCLI-D-20-0794.1.

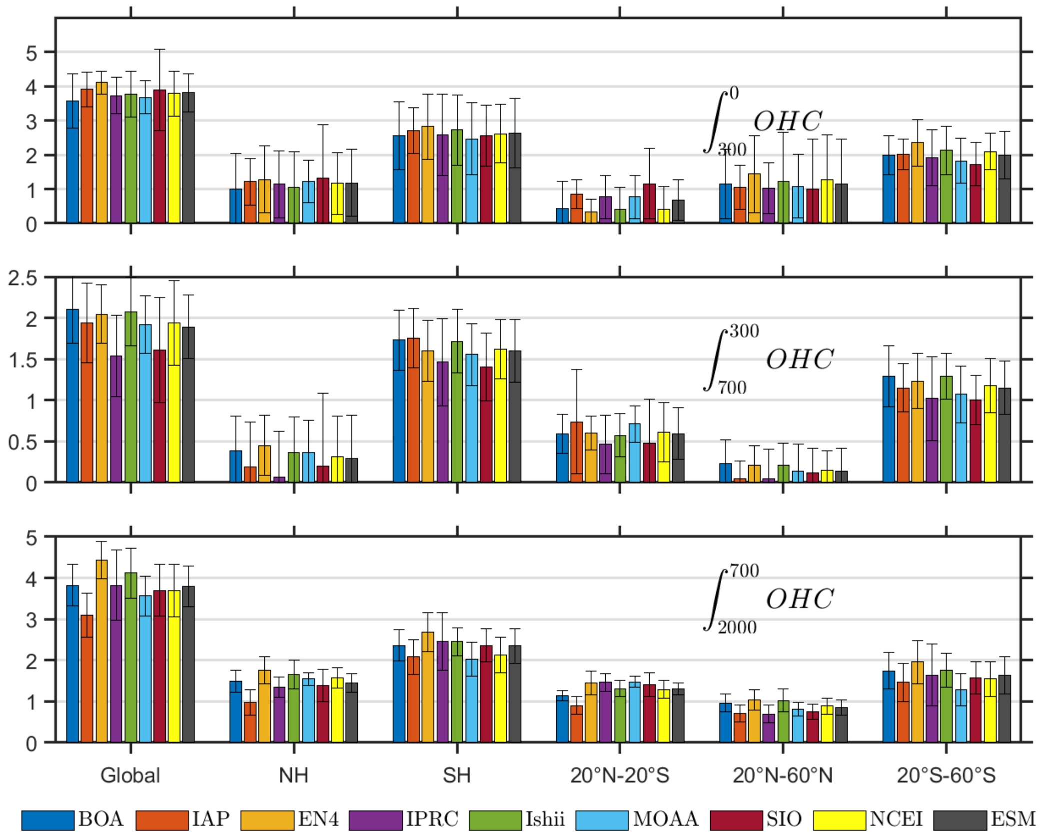

Fig. 5 Linear trend of the global and regional integrated OHC. The error-bar shows the uncertainty (±2σ). (Unit: 10^{21}J yr^{-1})

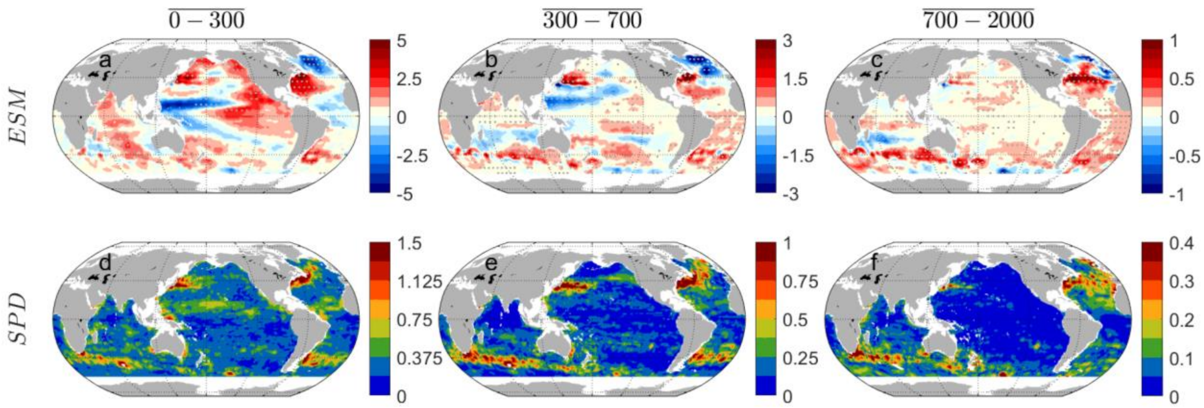

Fig. 6 OHC trends of the ensemble mean of depth-averaged OHC for the period 2005-2019. The statistically significant trends at 95% confidence level are highlighted by stippling. The corresponding spread is also given. (Unit: 10^5 J m^{-2} yr^{-1})

Accepted for publication in *Journal of Climate*. DOI10.1175/JCLI-D-20-0794.1.

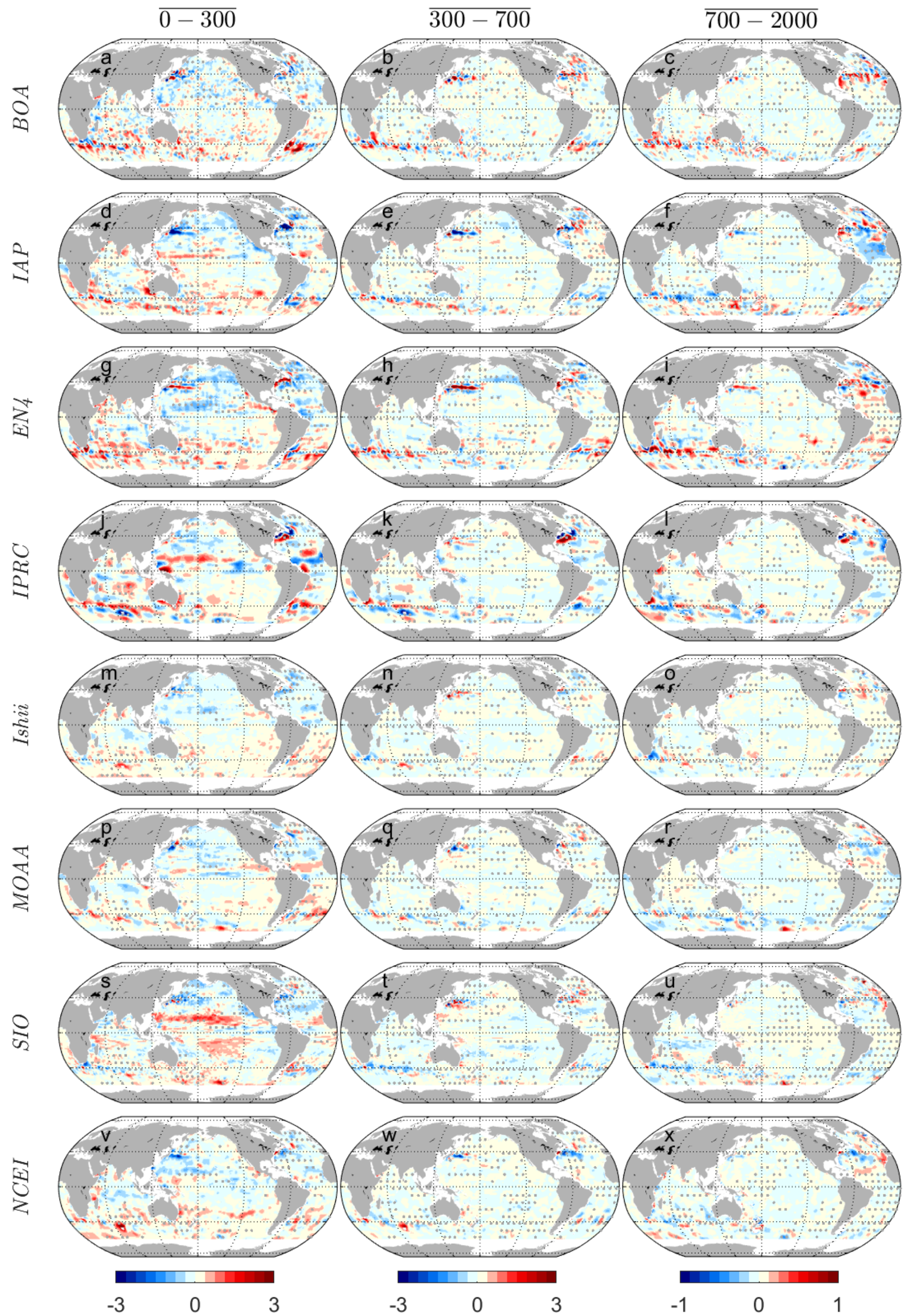

Fig. 7 Difference of OHC trends between each product and the ensemble mean. For each product, the statistically significant trends at 95% confidence level are highlighted by stippling. (Unit: 10^5 J m^{-2} yr^{-1})

Accepted for publication in *Journal of Climate*. DOI10.1175/JCLI-D-20-0794.1.

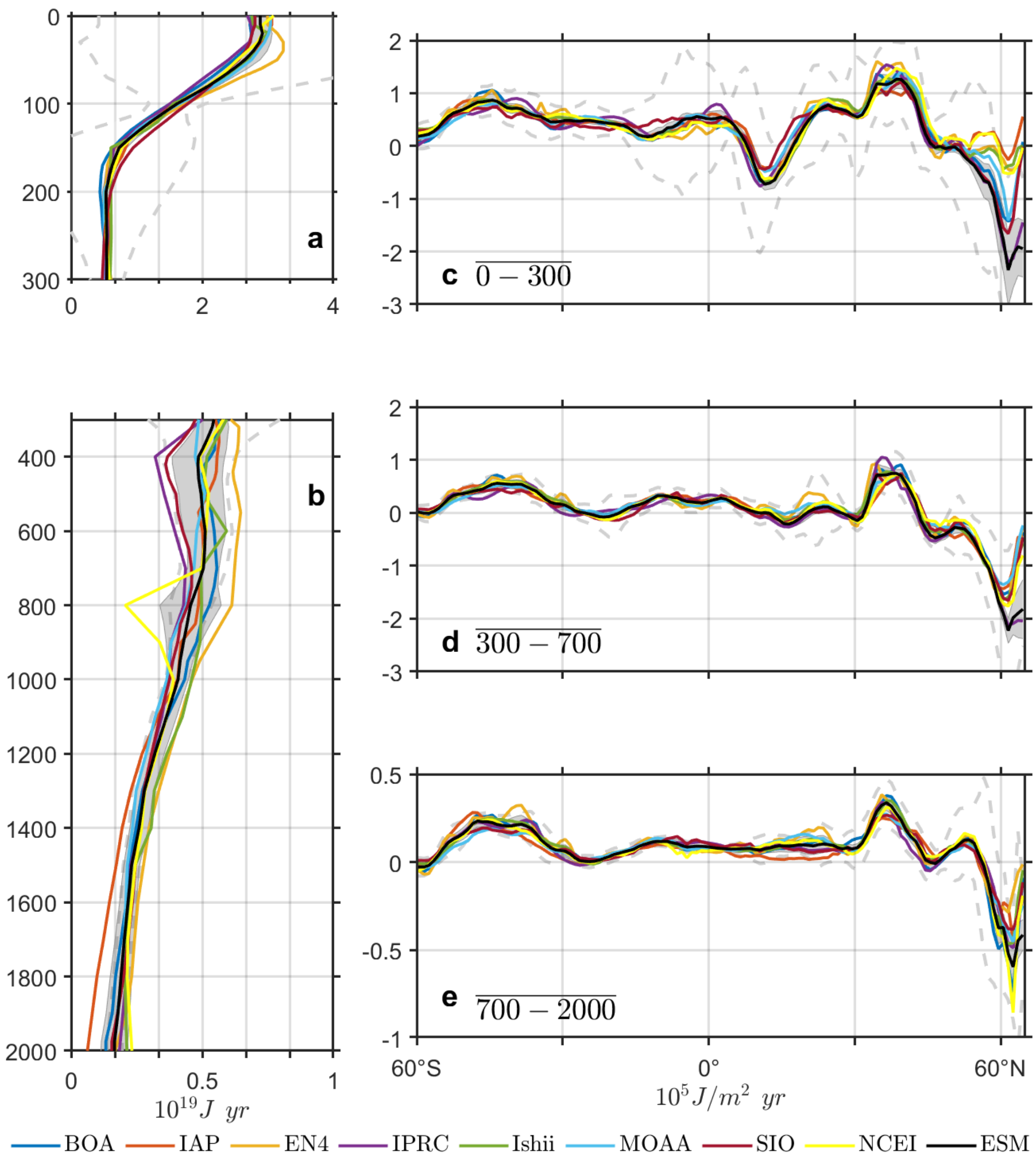

Fig. 8 (a & b) OHC trends for the global ocean at different depths. (c-f) OHC trends for zonal mean anomalies. Grey dashed lines mark the uncertainty of ESM at 95% confidence level. Grey shading is the spread of the trends. (Unit: 10^{19} J yr^{-1} for trends at depths, 10^5 J m^{-2} yr^{-1} for zonal trends)

Accepted for publication in *Journal of Climate*. DOI10.1175/JCLI-D-20-0794.1.

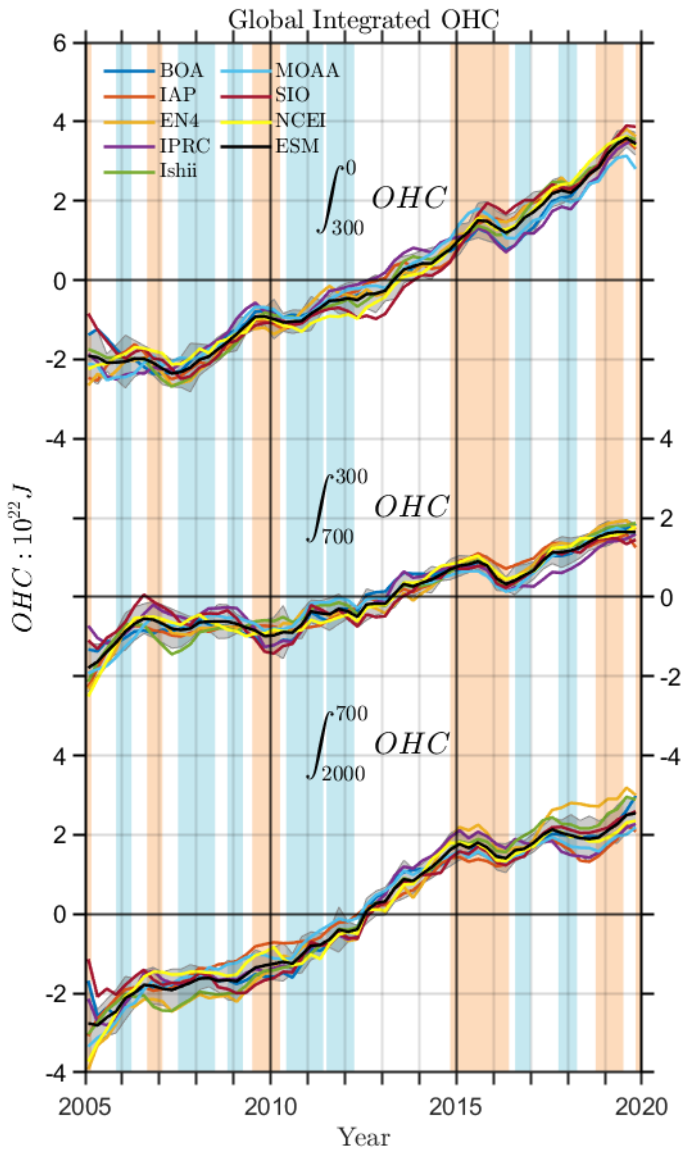

621 **Fig. 9** Monthly OHC anomaly time series globally and vertically integrated over the selected layers. Grey shading is the ensemble spread. Warm (tan) and cool (blue) ENSO events are marked based on a threshold of ± 0.5°C for the Oceanic Niño Index (ONI). (Unit: 10^{22} J)

Accepted for publication in *Journal of Climate*. DOI10.1175/JCLI-D-20-0794.1.

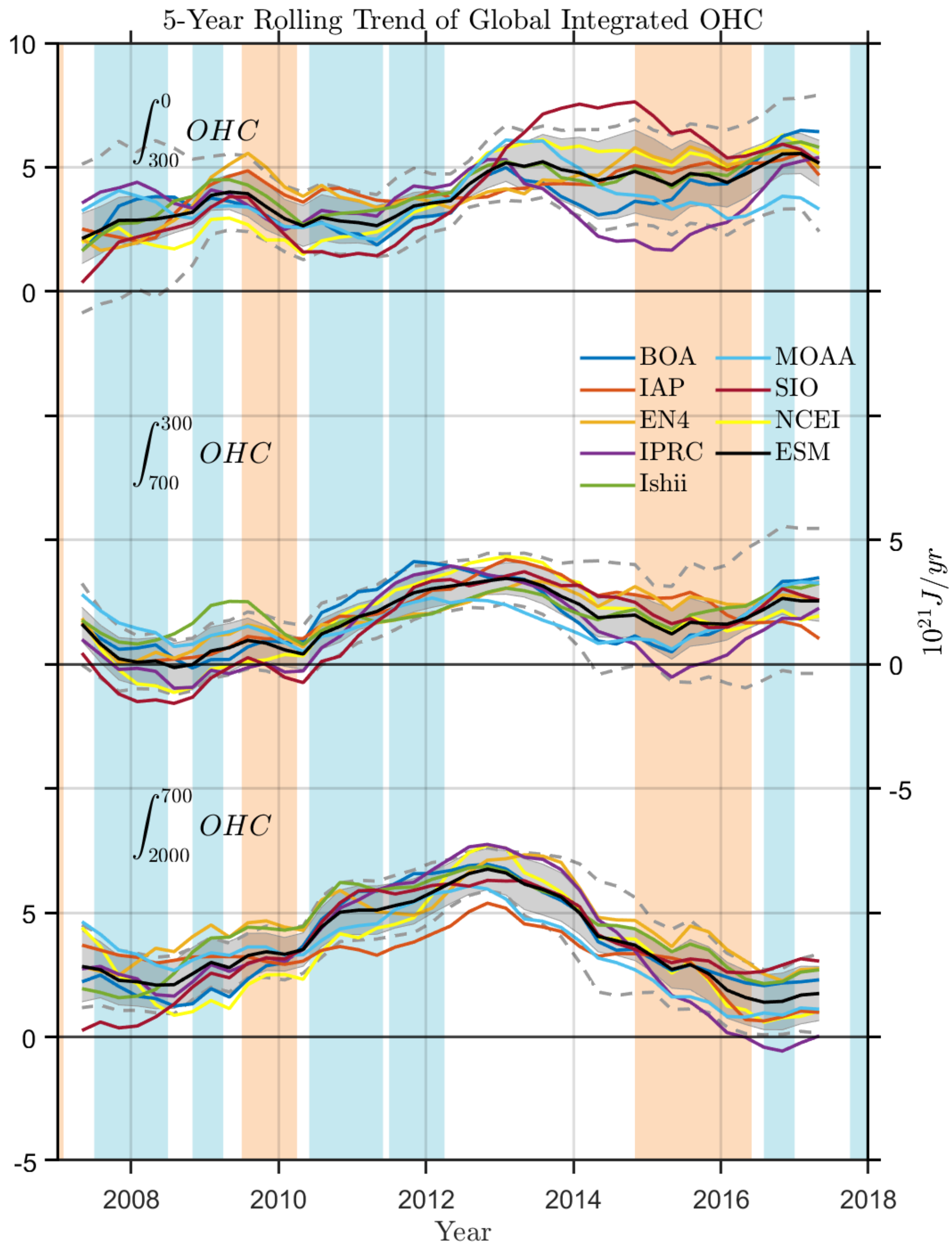

Fig. 10 The 5-year rolling trends of globally integrated OHC anomalies over the selected layers (plotted at the mid-point of each 5-year period). Grey dashed lines mark the uncertainty of ESM at 95% confidence level. Grey shading is the spread of the trends. Warm (tan) and cold (blue) ENSO events are marked based on a threshold of ± 0.5°C for the ONI. (Unit: 10^{21} J yr^{-1})

Accepted for publication in *Journal of Climate*. DOI10.1175/JCLI-D-20-0794.1.

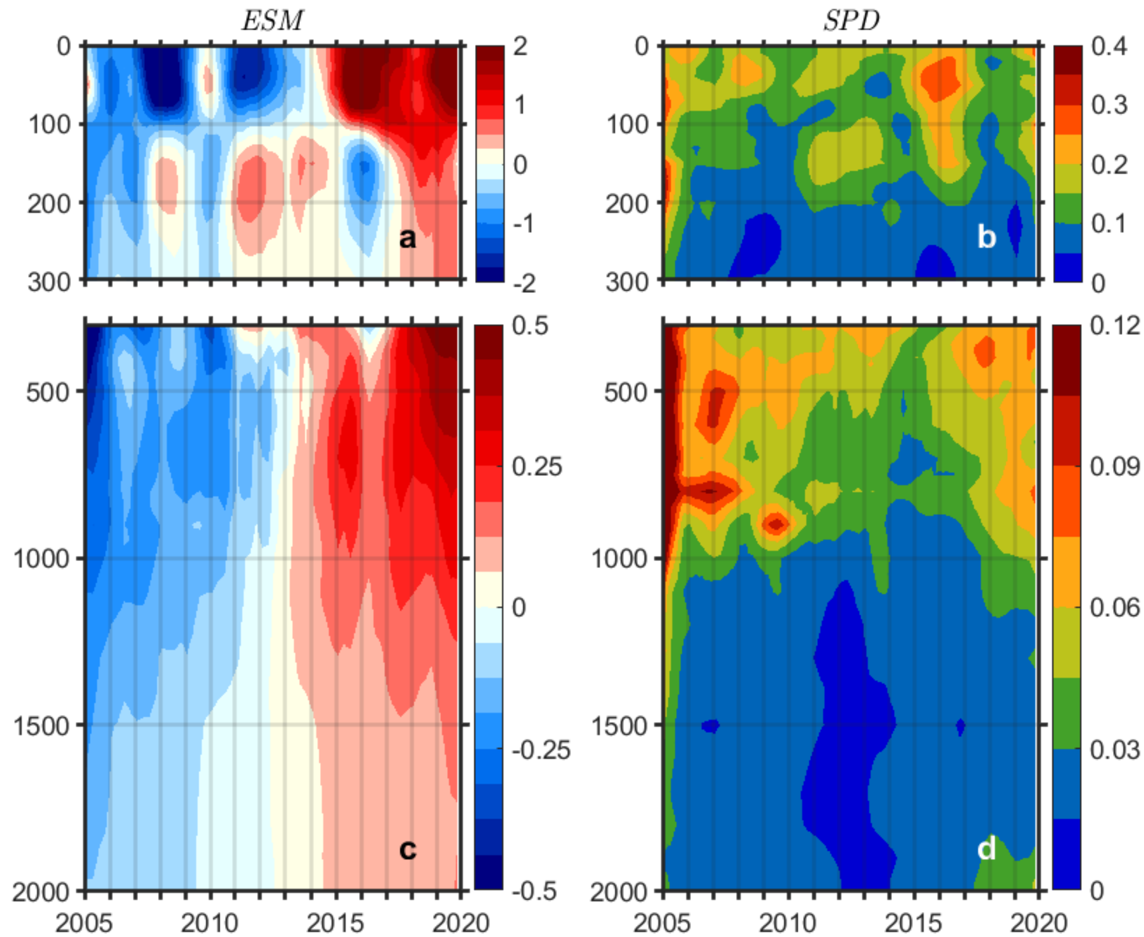

Fig. 11 Ensemble mean and ensemble spread of monthly evolution of the globally integrated OHC anomaly (Unit: 10^{20} J)

Accepted for publication in *Journal of Climate*. DOI10.1175/JCLI-D-20-0794.1.

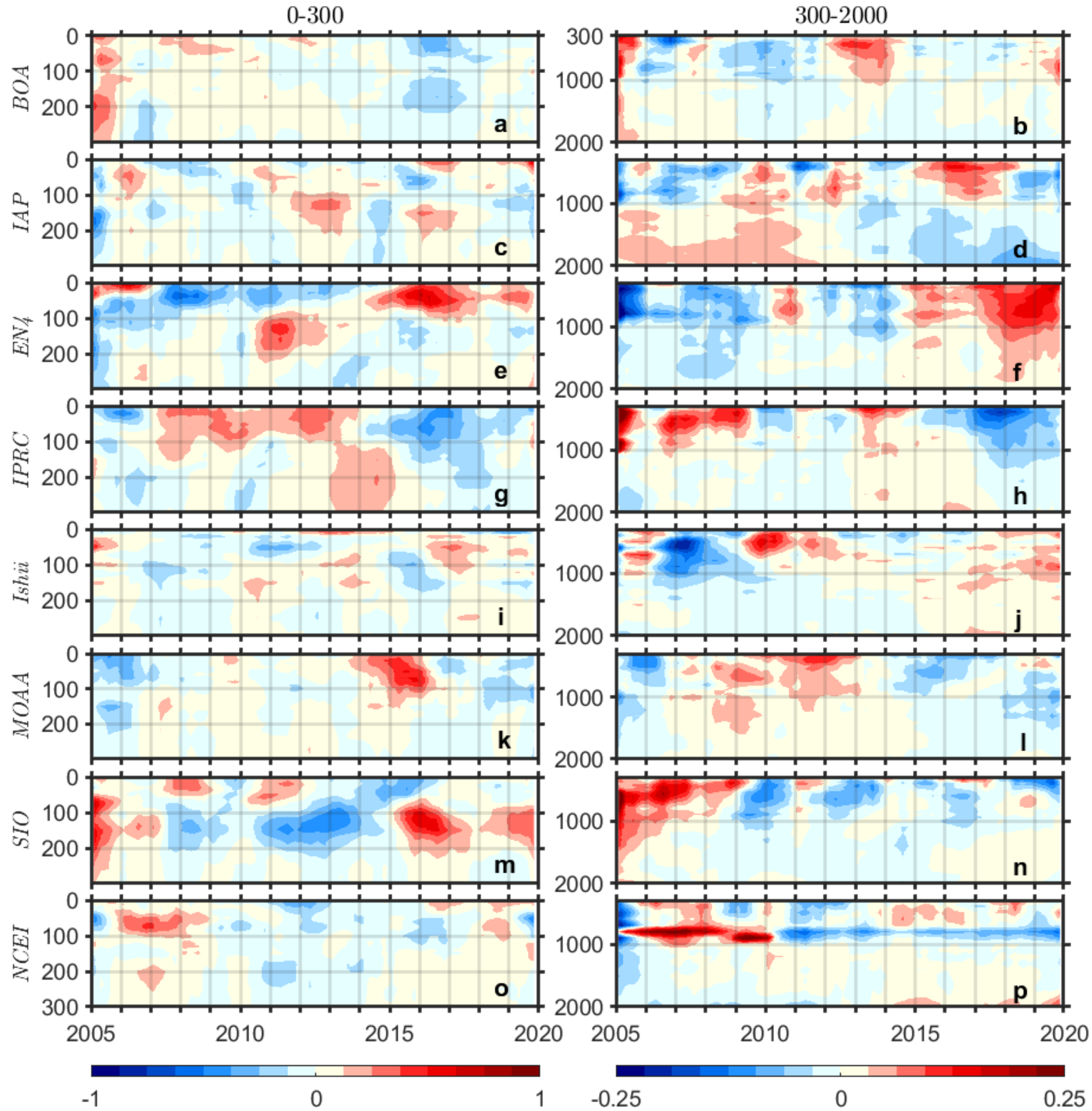

632

633 **Fig. 12** Difference of monthly evolution of OHC anomaly between each product and the

634 ensemble mean. (Unit: 10^{20} J)

Accepted for publication in *Journal of Climate*. DOI10.1175/JCLI-D-20-0794.1.

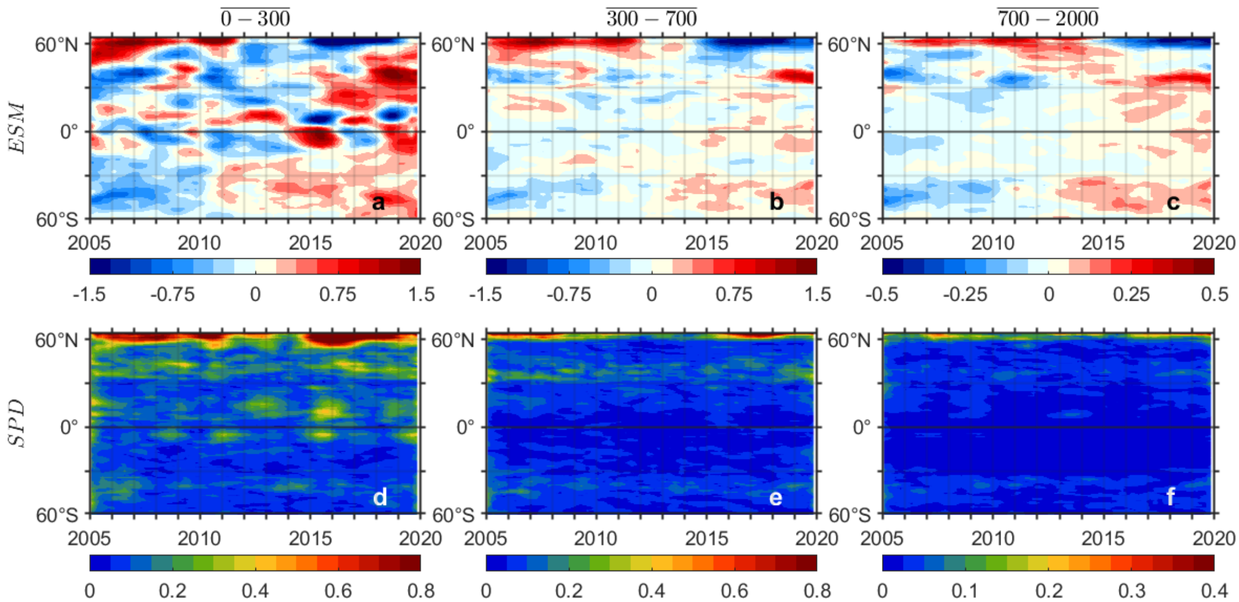

Fig. 13 Ensemble mean and ensemble spread of the zonal mean OHC anomaly. (Unit: 10^6 J m^{-2})

Accepted for publication in *Journal of Climate*. DOI10.1175/JCLI-D-20-0794.1.

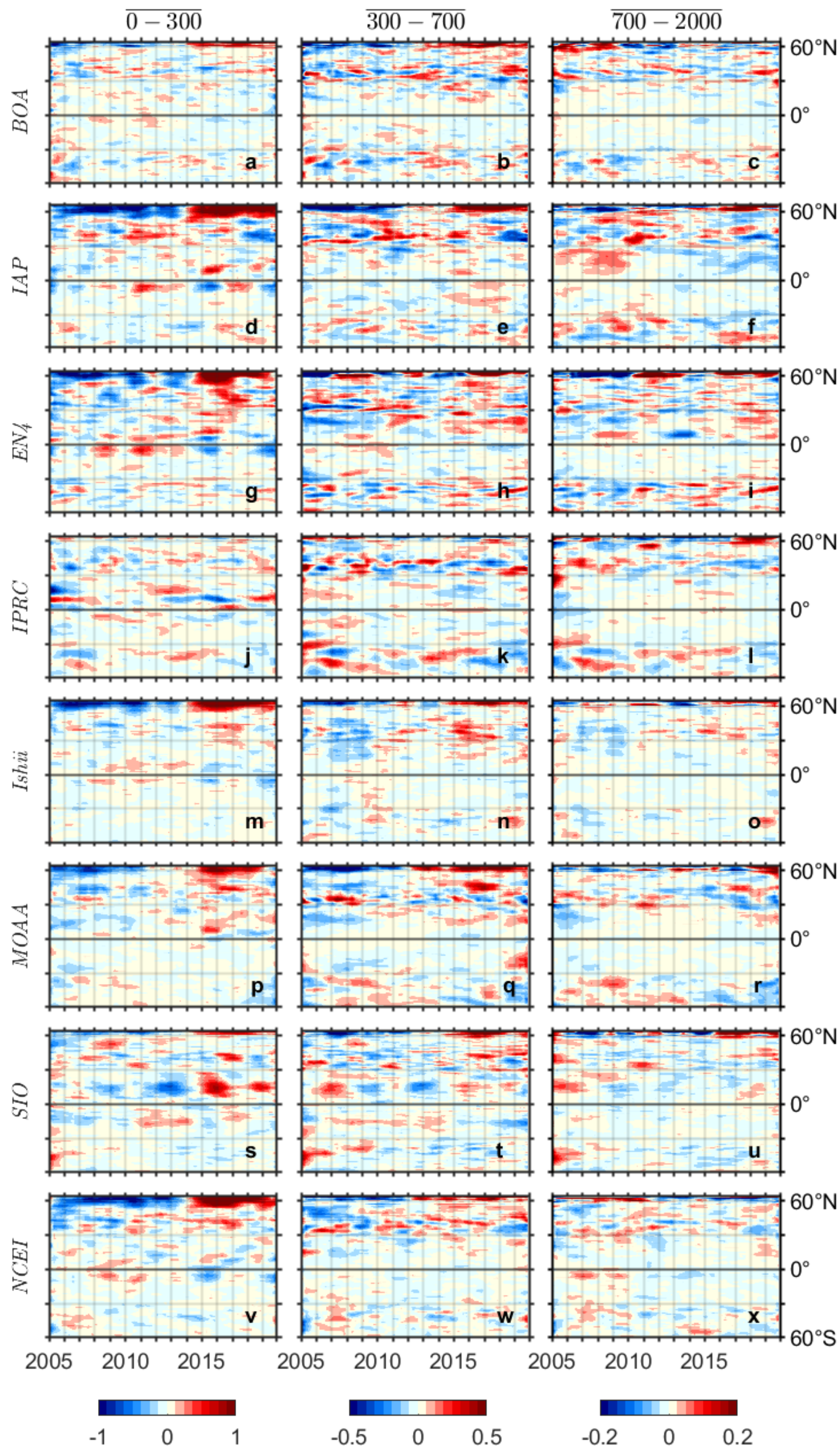

Fig. 14 Difference of zonal mean OHC anomaly between each product and the ensemble mean. (Unit: 10^6 J m^{-2})

Accepted for publication in *Journal of Climate*. DOI10.1175/JCLI-D-20-0794.1.

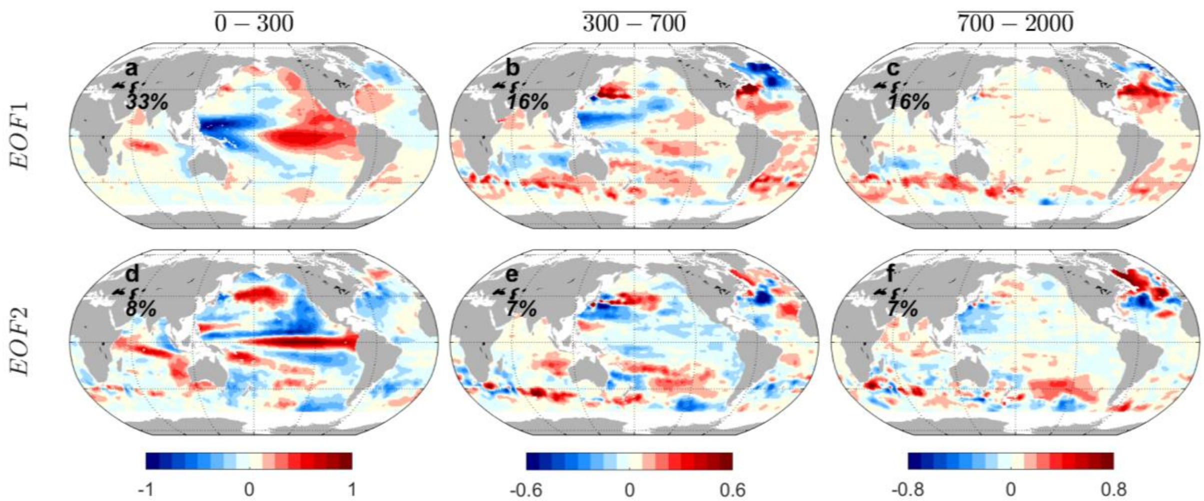

Fig. 15 Normalized first two EOF modes of depth-averaged OHC from the ensemble mean for the examined layers. The percentage of total variance explained by each EOF mode is provided. (Unit: m^{-2}).

Accepted for publication in *Journal of Climate*. DOI10.1175/JCLI-D-20-0794.1.

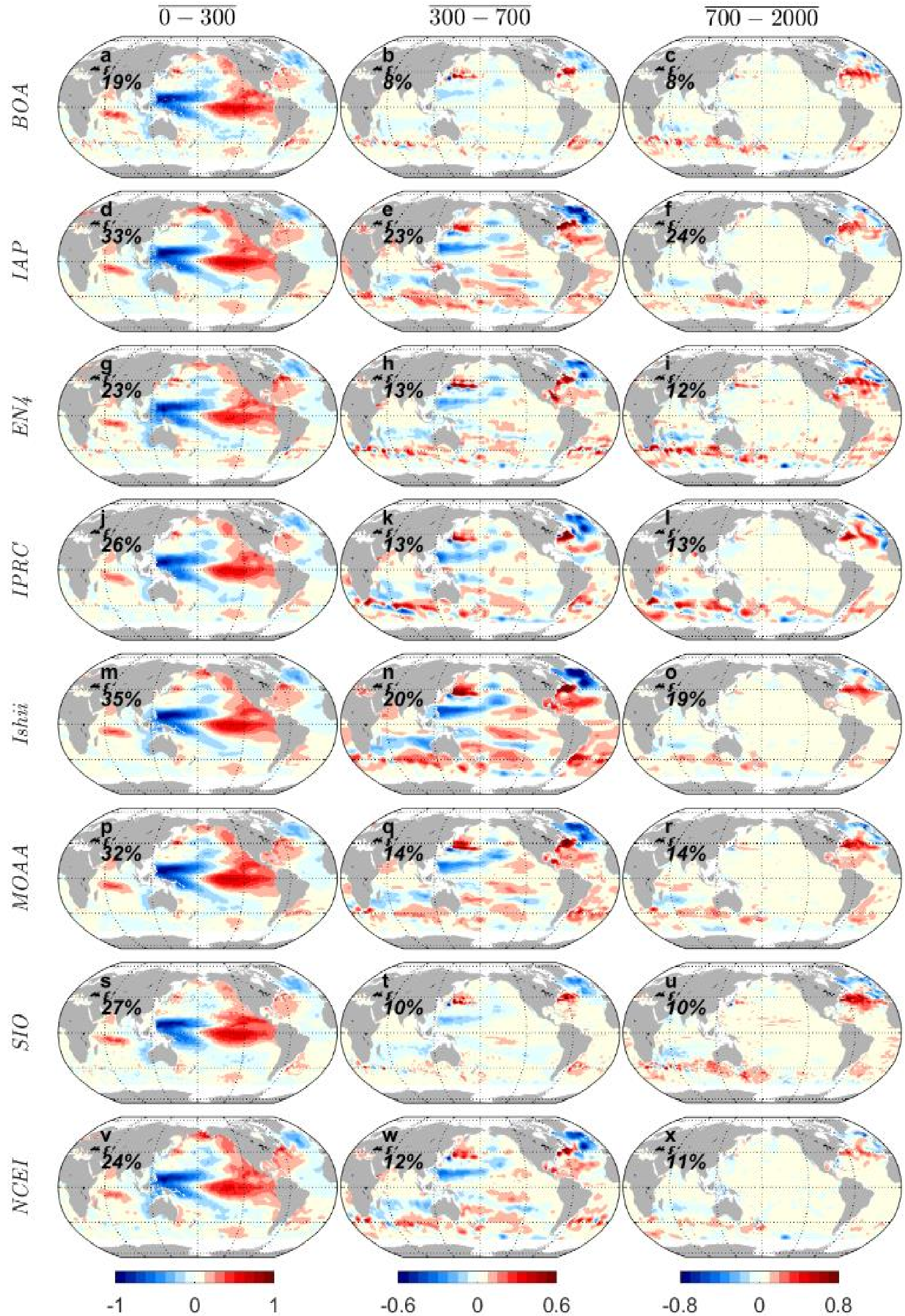

Fig.16 Normalized first EOF mode of depth-averaged OHC from the in-situ products for the examined layers. The percentage of total variance explained by each EOF mode is also provided.

Accepted for publication in *Journal of Climate*. DOI10.1175/JCLI-D-20-0794.1.

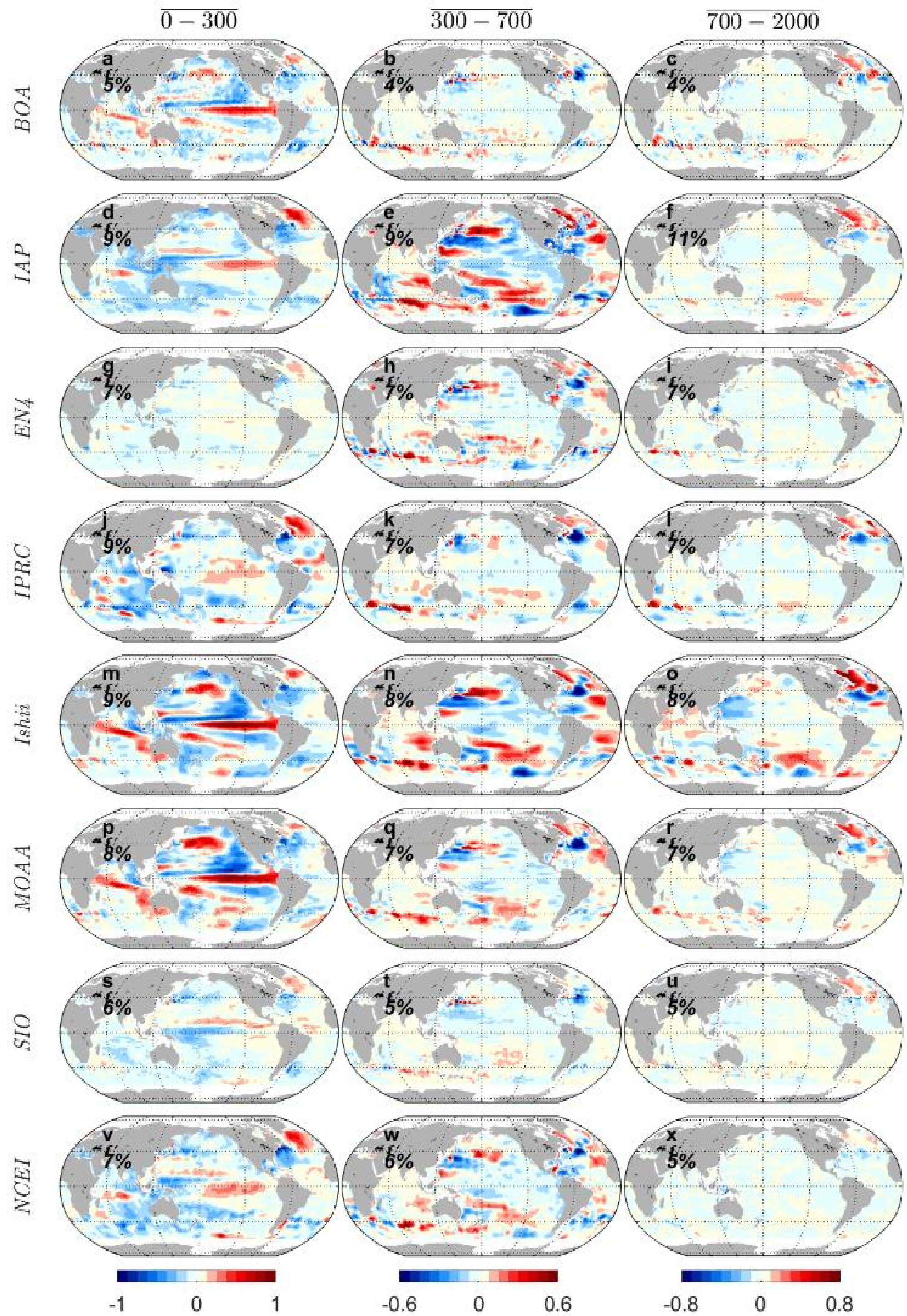

Fig.17 Normalized second EOF mode of depth-averaged OHC from the in-situ products for the examined layers. The percentage of total variance explained by each EOF mode is also provided.

Accepted for publication in *Journal of Climate*. DOI10.1175/JCLI-D-20-0794.1.

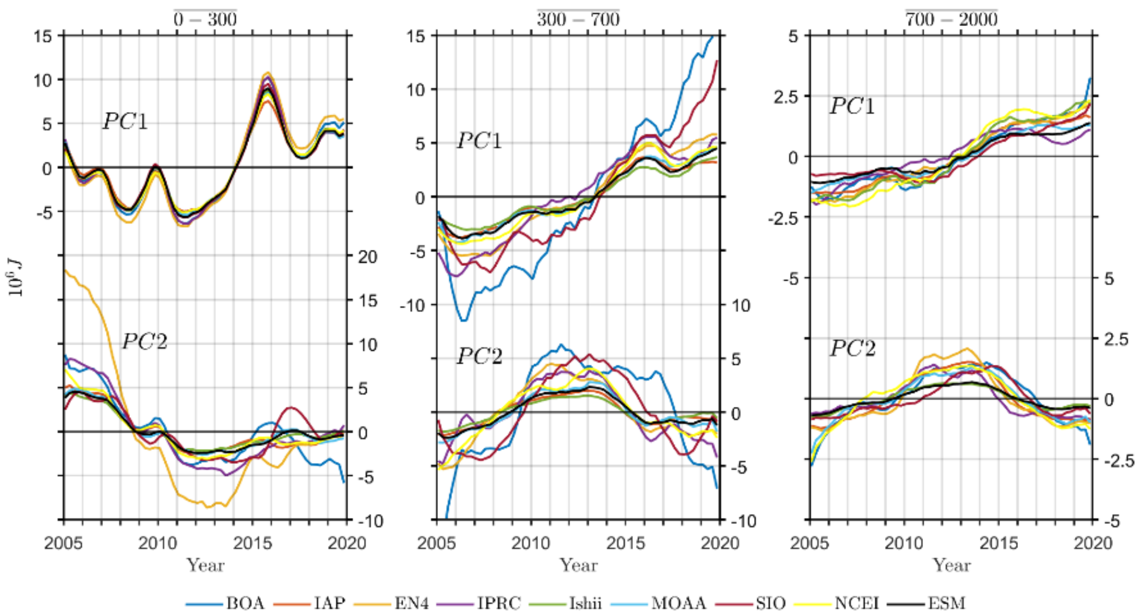

Fig. 18 Principal Components (PC) corresponding to the first three EOF modes for the examined layers from the in-situ products and the ensemble mean. (Unit: 10^6 J).

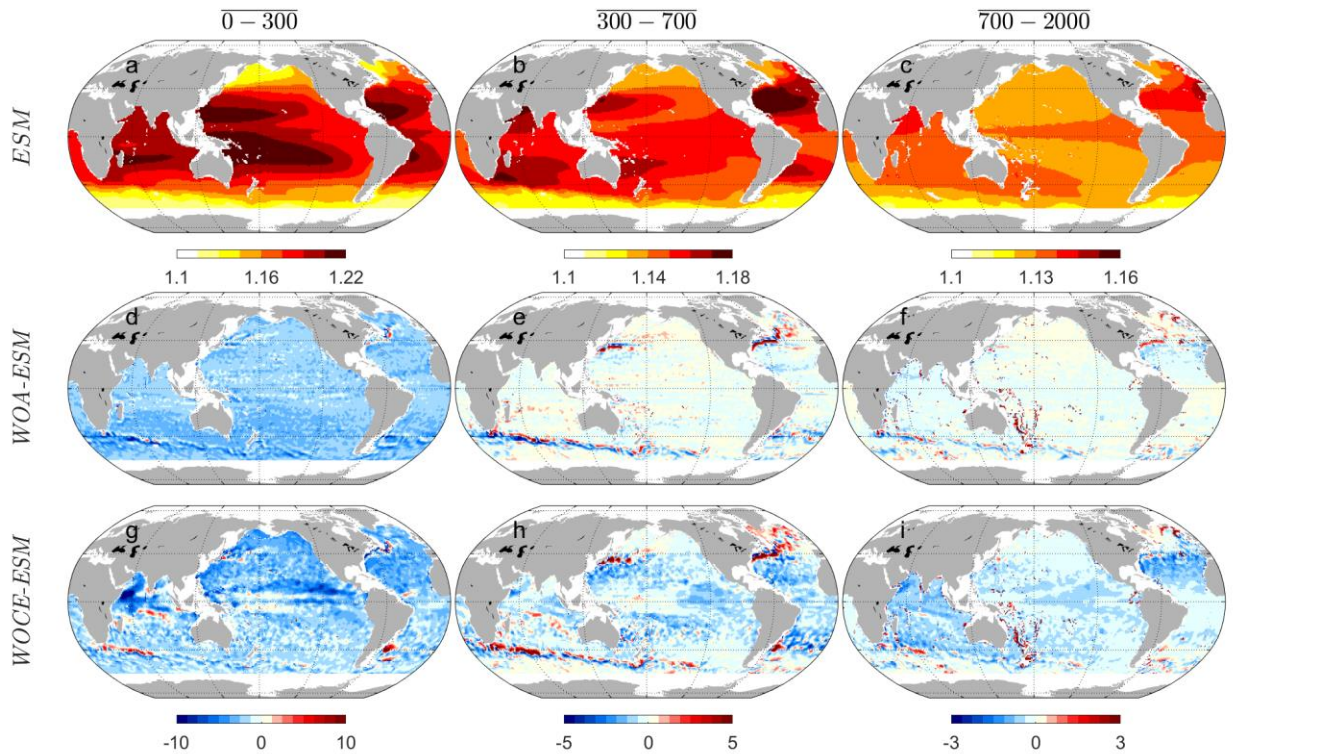

Fig. 19 (a-c) OHC Climatology from ensemble mean of the eight OA products (same as **Fig. 1**, a-c), and (d-i) difference in OHC climatology between high resolution products (WOA18 and WOCE-Argo, both of which were interpolated and subsampled at 1 degree) and the ensemble mean. (Unit: 10^9 J m^{-2} for the ensemble mean climatology, 10^6 J m^{-2} for the difference).

Accepted for publication in *Journal of Climate*. DOI10.1175/JCLI-D-20-0794.1.